RESEARCH ARTICLE

Key Points:
- Suprathermal Fe+ has been measured in Saturn's magnetosphere
- The source of the Fe+ might be impacting meteoroids or Saturn's dark material
- Suprathermal Fe+ appears to experience fewer losses than other ions near ~4 Rs

Supporting Information:
- Texts S1–S3, Tables S1–S3, and Figures S1–S15

Correspondence to:
S. P. Christon,
spchriston@aol.com

Discovery of suprathermal Fe+ in Saturn's magnetosphere

S. P. Christon[1], D. C. Hamilton[2], J. M. C. Plane[3], D. G. Mitchell[4], R. D. DiFabio[5], and S. M. Krimigis[4,6]

[1]Focused Analysis and Research, Columbia, Maryland, USA, [2]Department of Physics, University of Maryland, College Park, Maryland, USA, [3]School of Chemistry, University of Leeds, Leeds, UK, [4]Johns Hopkins University Applied Physics Laboratory, Laurel, Maryland, USA, [5]Department of Physics, University of Louisiana, Lafayette, Louisiana, USA, [6]Academy of Athens, Athens, Greece

Abstract Measurements in Saturn's equatorial magnetosphere from mid-2004 through 2013 made by Cassini's charge-energy-mass ion spectrometer indicate the presence of a rare, suprathermal (83–167 keV/e) ion species at Saturn with mass ~56 amu that is likely Fe+. The abundance of Fe+ is only ~10^{-4} relative to that of W+ (O+, OH+, H_2O^+, and H_3O^+), the water group ions which dominate Saturn's suprathermal and thermal ions along with H+ and H_2^+. The radial variation of the Fe+ partial number density (PND) is distinctly different from that of W+ and most ions that comprise Saturn's suprathermal ion populations which, unlike thermal energy plasma ions, typically have a prominent PND peak at ~8–9 Rs (1 Saturn radius, $Rs = 60,268$ km). In contrast, the Fe+ PND decreases more or less exponentially from ~4 to ~20 Rs, our study's inner and outer limits. Fe+ may originate from metal layers produced by meteoric ablation near Saturn's mesosphere-ionosphere boundary and/or possibly impacted interplanetary dust particles or the Saturn system's dark material in the main rings.

1. Introduction

Saturn's equatorial magnetosphere is dominated at <20 Rs (1 Saturn radius, $Rs = 60,286$ km) by local origin charged and neutral atoms and molecules. W+, the water group ions (O+, OH+, H_2O^+, and H_3O^+), along with H+ and H_2^+, dominates Saturn's magnetospheric plasma sheet and ring current populations [*Krimigis et al.*, 2005; *Sergis et al.*, 2007; *Thomsen et al.*, 2010]. W+ is currently understood to be mostly derived from one of Saturn's inner moons, Enceladus. Of four minor heavy ion species, C+, N+, O_2^+, and ^{28}M+, the first two atomic and the latter two molecular, the origin of only one, O_2^+, is known. (Please note that we use the textual construct ^{A}M^{+a} to denote a currently undetermined ion or set of ion species, *M*, which has a mass of A amu and a charge state of +*a*, where *a* is an integer, unless the ion is singly charged, in which case the charge state value 1 is typically suppressed.) In the case of ~28 amu, we do not know which of several molecular ion species dominates the ^{28}M+ observations [see *Christon et al.*, 2013, 2014a, referred to hereafter as papers 1 and 2, respectively]. In the case of ~56 amu, we are confident that ^{56}M+ is Fe+, the atomic ion at that mass, but in the course of this paper will use ^{56}M+ prior to and Fe+ after we present our identification of Fe+ as the species we observe. The dominant O_2^+ population originates at thermal energies from photolysis of ring ice, has intensity that varies seasonally, spreads to the outer magnetosphere, and is subsequently accelerated to hundred keV energies [see *Johnson et al.*, 2006 and paper 1, and references therein]. The minor ions are presumed to originate locally and have abundances relative to W+ of roughly ~10^{-2} [see *DiFabio*, 2012 and papers 1 and 2]. Saturn's suprathermal ion partial number densities (PND) typically peak radially at ~8–9 Rs, in the ring current region [*Sergis et al.*, 2007; *DiFabio*, 2012; paper 2]. The O_2^+ and ^{28}M+ PNDs vary seasonally, having apparent maxima near solstices and observed minima around equinoxes (see papers 1 and 2). W+, C+, and N+ variations are described elsewhere [see *Mauk et al.*, 2009; *DiFabio*, 2012]. ^{56}M+ can then be thought of as an additional tool for investigating and understanding ion sources, transport, and acceleration in planetary magnetospheres. As well as at Saturn, we have now observed suprathermal ^{56}M+ at Earth at radial distances from ~9 to ~30 Earth radii, RE, [see *Christon et al.*, 2014b]. While high charge state solar wind Fe$^{+8:+14}$ has long been known to be present in the near-Earth magnetosphere [*Christon et al.*, 1994], long-term collections now also reveal ^{56}M+ near Earth with no obvious charge exchange products between the solar wind Fe$^{+8:+14}$ and ^{56}M+. (Please note that we use the textual construct +*a*:+*b* to denote the range of charge states from +*a* to +*b*.) Below, we describe the relevant observations at Saturn, in particular, and of iron in planetary ionospheric and magnetospheric environs in general.

Interplanetary dust particles (IDPs, in which we include meteoroids, which are defined as particles larger than 5 μm in radius) [*Rubin and Grossman*, 2010], originating from comets and asteroids, impact all planets including Saturn and its rings. For example, ~16–60 tons of IDPs fall into Earth's atmosphere every day [*Plane*, 2012; *Gardner et al.*, 2014]. For simplicity, we will refer to all nonaqueous, infalling interplanetary material collectively as cosmic material in order to distinguish it from "ice dust," the micron- to nanometer-sized water ice grains that are present throughout Saturn's magnetosphere and in high-altitude noctilucent clouds at Earth. Because many types of cosmic material have a probability of containing some Fe, cosmic material is likely the original source of the Fe from which the Fe^+ at Saturn derives. (Note also that higher-energy charged particles, galactic cosmic rays or GCRs, also contain Fe and also impact Saturn's atmosphere and/or its rings producing secondary "splash" particles) [*Chenette et al.* 1980]. Higher-energy charged particles such as these are addressed below near the end of this section. Cosmic material impacting Saturn and Titan likely forms thin metallic layers in their ionospheres similar to those found at Earth, Venus, and Mars [*Withers*, 2012] and expected to be present at planets and moons with atmospheres [*Moses and Bass*, 2000; *Molina-Cuberos et al.*, 2001, 2008]. We note here that our focus in this paper is on Saturn, although Titan is also a likely source of meteoric metal ions [*Molina-Cuberos et al.*, 2001]. However, we do not consider Titan as important Fe^+ source as Saturn because of Saturn's much greater size (~550 times the surface area). At 80–90 km altitudes in Earth's ionosphere, near the mesosphere-ionosphere boundary, thin layers of ionized and neutral meteoric metals, including Mg, Fe, Na, Ca, and K, are produced by meteoric ablation, evaporation from the molten meteoroid [*Plane*, 2003]. The basis for our discussion of the ionospheric Fe^+ source herein is a model of the formation of a Fe/Fe^+ layer at Saturn with which we address nominal thermal, or Jeans, escape of Fe^+ from metal layers in Saturn's ionosphere. While the meteoric species are predominantly found in these layers, we are expressly interested here in their ionospheric escape after dispersal from these layers. Fe^+ at Earth, for example, has been detected at altitudes far from the metal layers, up to altitudes of ~1000 km near the equator and at varying concentrations from low to high altitudes at different local times and latitudes [*Grebowsky and Aiken*, 2002].

Outward flowing ion conics at energies from ~30 keV to ~200 keV accompanied by ~20 keV to ~1 MeV electron beams are measured throughout Saturn's outer magnetosphere [*Mitchell et al.*, 2009a]. They are observed at all local times on field lines that nominally map from well into the polar cap (dipole $L > 50$) to well into the closed field region ($L < 10$), strong evidence for ion and electron acceleration in Saturn's auroral zone. Saturn's south aurora sits ~1.5°–2° more equatorward and is wider than the north aurora as a result of the planetary magnetic dipole field's northward offset and has extremely variable boundaries. Two dedicated studies of the south auroral poleward boundary show consistent measures, where the south auroral colatitude (a) poleward (equatorward) edge ranges from 2° to 20° (6° to 23°) with median ~14° colatitude [*Badman et al.*, 2006, 2014] and (b) poleward (equatorward) full width at half maximum ranges from ~7.5° to 16° (16° to 25°) with median ~16° ± 2° [*Carbary*, 2012, Figure 3]. This allows outflows at times from the southern aurora's equatorward edge at latitudes of ~74° (~65°) access to approximate dipole L locations into ~13.2 (~6.0), where $L = \cos^{-2}(\Lambda)$ and Λ is the invariant latitude of the point where the L shell of a centered dipole intersects the planet (see Figure S14 in the supporting information and *Søraas* [1973]). The ion conics composition is typically dominated by light ions, with a few associated heavy ions, which flow exclusively outward. Associated electrons, measured by a different instrument, travel either outward, as do the ions, or bidirectionally. In one case, *Badman et al.* [2012] demonstrated upward bursts of 100–360 keV light ions and 250–600 keV heavy ions, as well as electrons with hundreds of keV energies, that mapped back to high-latitude intense auroral arcs separated by dark regions poleward of Saturn's northern dayside auroral oval in Saturn's cusp region [*Badman*, 2012]. Note that in the imaging and neutral camera, INCA, the sensor which measured the outflowing suprathermal ions [*Mitchell et al.*, 2009a; *Badman et al.*, 2012], hydrogen, and oxygen is well separated, but INCA's capability for higher mass discrimination is limited [*Mitchell et al.*, 2009a]; therefore, in discussions of the ion conics and beams, low mass species, H^+, H_2^+, H_3^+, and/or (possibly) He^+, are collectively referred to as "light" ions, and high mass species are referred to as "heavy" ions. The heavy ions are generically identified as "O^+," but they may include the carbon ions C^+, CH_3^+ (and other hydrocarbons, see, for example, the Saturn ionospheric chemistry of *Moses and Bass* [2000]), CO^+, CO_2^+, OH^+, H_2O^+, and/or Fe^+ (and/or other meteoric ions such as Na^+, Mg^+, and/or Si^+).

Outflowing suprathermal ions at Saturn may result from ionospheric processes similar to those observed at Earth, although the characteristic energies reported at Saturn are a factor of ~100 greater than those at Earth. These ion conic observations highlight that, in addition to the process of continual ion escape, there are likely

two high-latitude, planetary magnetic disturbance-related dynamic escape locations known at Earth, the dayside cleft ion fountain and nightside auroral outflow, which probably have active analogs at Saturn. At Earth, gravitation disperses low-velocity outflowing ions spatially, but separation of light and heavy escaping ions probably does not occur at Saturn because the escape velocity of Saturn's outflowing ions is about 3 times that at Earth. There are also powerful ionospheric escape events, reported at Earth and referred to as ionospheric mass ejections (IMEs) [*Moore et al.*, 1999], that often contain appreciable amounts of the molecular ions N^{+2} and NO^+ [*Wilson and Craven*, 1998], molecular ions that we observe in Earth's magnetosphere [*Christon et al.*, 1994, 2014b]. These IMEs are known to be initiated by CMEs that significantly disrupt Earth's magnetosphere [*Moore and Khazanov*, 2010; *Moore et al.*, 1999]. Below, we will refer to all these ionospheric escape processes collectively as ionospheric outflow because, even at Earth, details of processes in and/or contributions from ionospheric outflow regions are not necessarily well-enough studied and/or correlated with common indicators of solar or geomagnetic activity. They are still not fully understood [see, e.g., *Chandler et al.*, 1991; *Horwitz and Moore*, 1997; *Moore et al.*, 2014].

Cosmic material has been observed impacting Saturn's main rings by Cassini [*Tiscareno et al.*, 2013] and, as such, it likely contributes to and may even dominate the impurity composition of the main ring ices. Solstice and equinox temperatures of Saturn's main rings, at ~80–120 K and ~45–70 K, respectively [*Flandes et al.*, 2010], are generally colder than those in Earth's atmosphere at altitudes of ~95 km in the *E* region where a layer of meteoric Fe^+ has long been observed and modeled [*Carter and Forbes*, 1999; *Grebowsky and Aikin*, 2002; *Feng et al.*, 2013]. Whether the source region at Saturn is the main rings or its ionosphere, a large fraction of cosmic material contains varying amounts of metallic Fe, iron oxides, and/or minerals containing the elements Fe, Mg, Na, K, C, Ca, and/or Si [*Kopp*, 1997; *Anders and Grevesse*, 1989; *Jessberger et al.*, 2001; *Plane*, 2012]. Iron is a major element in most classes of meteorites [*Mason*, 1979]. Small IDPs also contain iron, as evidenced directly by Cassini's cosmic dust analyzer, CDA, observations during the cruise to Saturn in which two of the six small IDPs whose composition could be determined were found to be iron rich [*Hillier et al.*, 2007a]. Olivine (which has the collective formula $(Mg_x Fe_{1-x})_2 SiO_4, 0 \leq x \leq 1$), metallic Fe-Ni, and various iron oxides and Fe-inclusive minerals are present in cosmic material [*Rubin*, 1997; *Bridges et al.*, 2010]. Likely sources of Fe and $Fe_m O_n$ (wüstite, FeO, hematite, Fe_2O_3, and/or magnetite, Fe_3O_4) are reduced or oxidized iron-containing compounds in the cosmic materials in interplanetary space which are believed to be generated in large part by asteroid belt collisions [*Grebowsky and Aikin*, 2002; *Grün et al.*, 2001; *Hutchison*, 2007; *Plane*, 2012].

Local origin charged and neutral ice particles, gas clouds, and atomic and molecular heavy ions play active roles in Saturn's magnetosphere. Early in the Cassini mission it was noted that, while the ultraviolet imaging spectrograph measurement of the rings' reflectivity showed the main rings becoming brighter from the C ring to the A ring, the visual and infrared mapping spectrometer (VIMS) instrument data showed the outer A ring to be richer in the "mystery" iron-based silicate dark material [*Miner et al.*, 2007]. *Jaumann et al.* [2009] noted that the dark material appears throughout Saturn's system, most predominantly on Dione (~6.3 *Rs*), Rhea (~8.7 *Rs*), Hyperion (~24.5 *Rs*), Iapetus (~59 *Rs*), and Phoebe (~215 *Rs*). Additionally, Cassini discovered plumes of water vapor and icy material being ejected from large fissures at the south pole of the moon Enceladus. Enceladus' orbit is at ~3.95 *Rs*, and its ejecta contribute over time to form Saturn's E ring and OH torus. Long-term CDA measurements have detected *E* ring particles far beyond the classical, optically determined 3–8 *Rs* equatorial E ring, that is, ~2–4 *Rs* away from the ring plane, outward to ~20 *Rs*, and inward almost to the outer edge of the A ring [see, e.g., *Srama et al.*, 2011, Figure 10]. Icy matter between the F ring (~2.33 *Rs*) and the outer edge of the A ring (~2.27 *Rs*) extinguishes the radiation belts [*Kollmann et al.*, 2011]. The Enceladus neutral cloud torus, fed by the moon's plumes and centered on its orbit, is the densest part of the E ring [*Cassidy and Johnson*, 2010] and is the second largest structure in the Saturn system next to the 40 *Rs* thick Phoebe ring at ~128–207 *Rs* [*Verbischer et al.*, 2009].

Some matter from the E ring and the Phoebe ring appears to have common characteristics with ice contaminants on or in other objects, rings and moons, in the Saturn system. Micron-sized and smaller E ring particles from Enceladus (also called grains and dust) are mostly pure water ice, but some, a few percent, have small amounts of contaminants such as silicates, CO_2, NH_4, N_2, and hydrocarbons [*Hillier et al.*, 2007b; *Postberg et al.*, 2008; 2011]. CDA data show that ~98% of all resolved E ring icy particle mass spectra are dominated by water and water cluster ions, $H–(H_2O)_n^+$, and another <1% of their observations represent meteoric metals [*Postberg et al.*, 2008]. *Postberg et al.* [2008] note that with water clusters dominating most E ring spectra, the CDA cannot detect minor

contributions of Fe^+ in Saturn's environs as a result of a prominent water cluster, $H\text{-}(H_2O)_3^+$, at ~55 amu. CDA also observes various $H^+\text{-}$ and $Na^+\text{-}$water cluster peaks at ~59, ~63, ~77, and ~77 amu, some with amplitudes comparable to or greater than the peak at ~55 amu [*Postberg et al.*, 2008]. *Waite et al.* [2006, 2009] identify neutral species count distributions they observe in the ~50–60 amu range as C_4 hydrocarbons. To our knowledge, there are no other reports of species in the ~50–60 amu range. If there is any Fe and/or Fe^+ in the Enceladus plumes possibly hidden by these water clusters and/or hydrocarbons, it will likely experience the same fate as the other Enceladus materials we discuss below. From their model of Enceladus origin water-based ions and neutrals in the inner magnetosphere, *Jurac and Richardson* [2007] estimated that ~17% of the dense neutral water products from Enceladus is deposited mostly onto the A ring, but the atomic and molecular water cloud particles probably reach all the main rings through ion-neutral scattering and ring particle collisions. *Clark et al.* [2012] find that dark material from Phoebe's ring has spectral characteristics in common with the contaminants in Saturn's icy main rings and its moons, suggesting that some of Phoebe's dark material may reach the main rings, in particular, over time.

Saturn's main rings are primarily composed of constantly interacting water ice bodies of various sizes, from nanometer- to boulder-sized objects and constantly changing clumps of the same. The main rings are visually an overall pale tan color with a reddish tint, especially the A and B rings [*Estrada and Cuzzi*, 1996; *Cuzzi et al.*, 2009]. Ring ice appears to have a small (up to a few percent) contamination by UV-absorbing nonaqueous material, which includes as a constituent, or is, Saturn's so-called dark material [*Cuzzi et al.*, 2009; *Filacchione et al.*, 2012; *Clark et al.*, 2012]. *Cuzzi et al.* [2009] reviewed various ring composition studies, noted that the ring contaminants have been ascribed to both organic and inorganic materials, discussed the pros and cons of the various source options, and demonstrated that a compositional interpretation for the UV absorber including nanohematite explains the observations better than an absorber having organics alone. Hematite is the iron ore that gives Mars and red earths their color [*Morris et al.*, 1997]. *Filacchione et al.* [2012] devoted their study to investigating organic compounds as the prime contaminant sources and found that organics could explain the UV absorber, but they did not compare the pure organic fits to alternate inorganic(hematite)-inclusive contaminant fits. *Clark et al.* [2012] found that the dark material appears to have significant components of nanophase metallic iron and nanophase hematite contributing to the observed UV absorption. By modeling both the ice and dark contaminant grain size distributions, *Clark et al.* [2012] demonstrated that multiple spectral features and the overall spectral shape of the dark material on Phoebe match those seen on the dark side of Iapetus, a few other moons, Saturn's rings Cassini Division, and the F ring, thus implying the material has a common composition throughout the Saturn system. After investigating many substances, *Clark et al.* [2012] concluded that the dark material could be a mixture of nanophase metallic iron (Fe), nanophase hematite (Fe_2O_3), CO_2 and H_2O, with possible traces of ammonia (NH_4), bound water, H_2, or OH-bearing minerals, trace organics, and other as yet unidentified materials. This mixture was found to be a simple and consistent explanation for the dark material in Saturn's environs. Taken together, these studies suggest that the contaminants in Saturn system ice with reddish tints likely have amounts of nanophase metallic iron and nanophase hematite.

Summarizing the current information on Saturn's rings, Cassini VIMS finds visual reddening in the A and B rings much stronger than that of the C and D rings or any of the other icy satellites, except possibly Rhea or Hyperion [*Filacchione et al.*, 2012; *Cuzzi et al.*, 2009]. *Clark et al.* [2011] find that nanophase hematite and nanophase metallic iron in a mixture with fine-grained water ice and other materials are the most likely explanation for the spectral structure of the contaminant in the icy surfaces of the Saturn system. Notably, *Clark et al.* [2012] find that organic compounds, such as tholins, do not match the observed spectra as well as the tested mixture of nanophase iron dominated materials. Because of the abundance of water ice in the Saturn system, oxidation of metallic iron and wüstite, common components in meteorites, might be expected.

Unlike charged and neutral thermal energy atomic and molecular populations whose intensity maximum can often help identify a nearby source location, intensities of suprathermal ions are often determined by magnetospheric dynamics far from their origin. Ionospheric ions can propagate far away from their origin throughout the magnetotail, where they can be accelerated to keV energies in the crosstail current sheet followed, at times, by redistribution to distant locations in minutes or hours. Consequently, suprathermal ions from various sources are often thoroughly mixed by the time they are measured.

Several other possible Fe source candidates are briefly addressed here (an extended discussion and reference list is in section K of the supporting information). As noted above, MeV energy ions and electrons over the
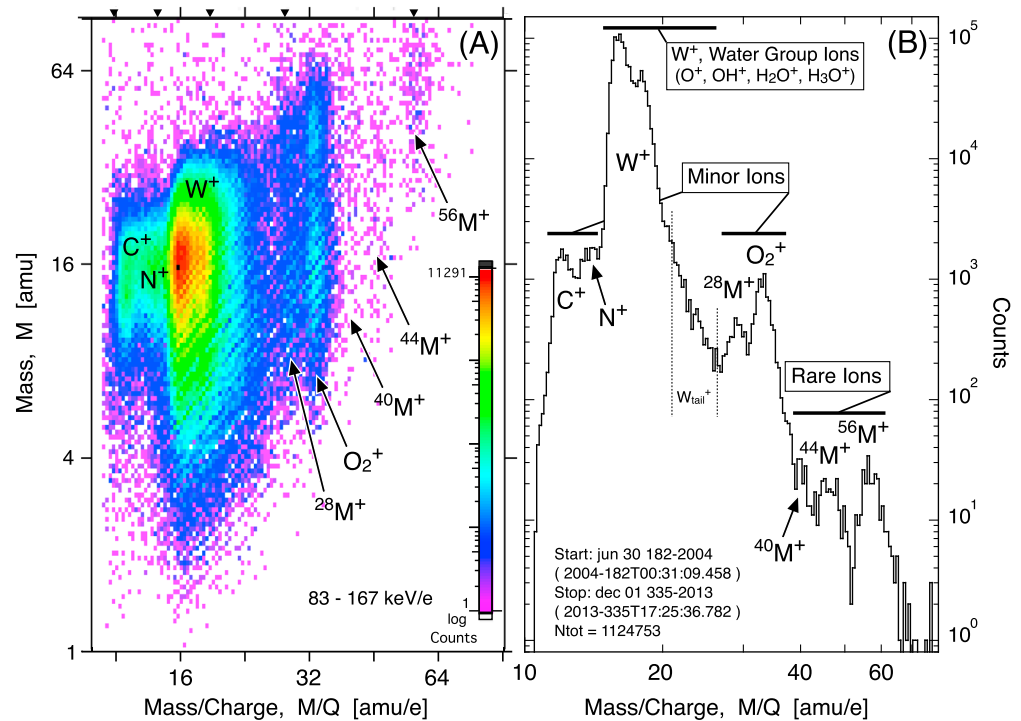
Figure 1. (a) Triple coincidence pulse height analysis events (PHAs) measured in Saturn's near-equatorial magnetosphere under our selection criteria (see text) inside of 20 R_s or the magnetopause, whichever is closer to Saturn, from SOI (2004–181) through calendar year 2013 are displayed in a Mass, M, versus Mass per Charge, M/Q, color spectrogram. The water group, W^+ (mostly O^+ at 16 amu/e, followed by roughly equal amounts of OH^+ and H_2O^+ at 17 and 18 amu/e, respectively, at about half the O^+ abundance, along with a little H_3O^+), and the minor and rare heavy ion species are identified. The small triangles above the top axis identify the expected M/Q location of the lowest five charge states of Fe, with Fe^{+5} (Fe^{+1}) being furthest to the left (right). (b) Histogram of the PHA data plotted in Figure 1a. The histogram permits clearer identification of the rare ion group $^{56}M^+$ and facilitates qualitative visual comparisons to W^+ and the minor ions. W_{tail}^+, a section of the straggling tail of the water group peak (22–26 amu/e), is used to monitor the W^+ background level in the minor and rare ions (see text).

main rings are consistent with modeled splash albedo production resulting from bombardment of Saturn's atmosphere and/or its rings by high-energy GCRs. Some portion of these secondary ions, or even the primary GCRs, might ultimately lose energy through successive collisions and charge exchanges to be observed at low-charge state and hundred keV energies. A review of the literature (see section K of the supporting information) shows that $^{56}Fe^{+Q}$ ions are reported in both fast ($Q_{Fe,HSSW} = 7–12$) and slow ($Q_{Fe,LSSW} = 8–14$) solar wind, SW, from lower and higher in the Sun's corona, respectively; the corotating interaction regions, CIR, that form between fast and slow solar wind streams; solar energetic particle (SEP) events ($Q_{Fe,SEP} = 8–16$) from solar flares; coronal mass ejections, CME ($Q_{Fe,CME} = 10–22$), large-scale outbursts of solar wind plasma and magnetic fields more massive than individual solar flares; galactic cosmic rays, GCR ($Q_{Fe,GCR} = 26$), from the interstellar medium; and finally, the low-charge state anomalous cosmic rays, ACR ($Q_{Fe,ACR} \geq 1$), and singly charged inner source pickup ions, ISPUI ($Q_{Fe,ISPUI} \geq 1$), from interstellar gas, dust, and grains. GCR Fe ions are likely fully stripped, as are probably all GCR ions. CME Fe ions have the highest charge states of solar origin Fe, $10 \leq Q_{Fe,CME} \leq 22$. For any of the galactic or solar origin ions, GCR, CME, SEP, CIR, and SW, to charge exchange down to $Q_{Fe,SW} = 1$, charge exchange products should leave a trail of intermediate charge state Fe ions between their original Q values at $7 \leq Q_{Fe} \leq 26$ (at 8 to 2.15 amu/e, where we would observe them) to $Q_{Fe} = 1$ (at 56 amu/e). Solar and/or galactic Fe might, through multiple charge exchange collisions, arrive at lower charge states. In section 3, we demonstrate that Fe at charge states intermediate between those of the solar wind ($7 \leq Q \leq 14$) and Fe^+ are not observed, so that high charge state GCR, CME, SEP, CIR, and/or SW ions are not Fe^+ sources. Upon discovering ~56 MeV Fe^+ at low L values in Earth's trapped radiation belts, *Mazur et al.* [1999, 2000, 2008] attributed this population to the ISPUIs and not to ACRs. However, Fe^+ has not been definitively identified in the ISPUI population, and the trapped Fe^+ might have another explanation (originating from the ionosphere in a process similar to the one we suggest for Saturn, for example). We conclude that

neither ACR Fe^+ nor ISPUI Fe^+ seems to be supported by a set of repeatable, persistent observations of the Fe^+ component. They are only attributed by possible identifications which are not supported by subsequent studies or independent observations. The interested reader can read our extended discussion, and reference list supporting this conclusion is in section K of the supporting information. Therefore, we conclude that none of the higher-energy solar and/or extrasolar candidates appear to be viable sources for the Fe^+ at Saturn.

Below we investigate the singly charged heavy atomic ion species, $^{56}M^+$, likely ionized and accelerated in Saturn's magnetosphere. Our study spans ~9.5 years of the Cassini mission. In the following sections, we describe the instrument and trajectory, the observations, and then compare and contrast our current understanding of possible suprathermal Fe^+ sources.

2. Instrument and Trajectory

The charge-energy-mass spectrometer (CHEMS) of the Cassini magnetospheric imaging instrument measures ~3–220 keV/e positive atomic and molecular ions [*Krimigis et al.*, 2004]. CHEMS uses energy per charge filtering followed by measurements of time of flight (TOF) and, at higher energies, kinetic energy (KE) with solid state detectors (SSDs). In this study, we use higher-energy data, the 83–167 keV/e range, in which ions trigger the SSD and mass per charge (M/Q) and mass (M) can both be determined [*Krimigis et al.*, 2004]. The triple coincidence (Triples) events resulting from the start and stop TOF pulses and the SSD pulse produce our lowest background data, which is required for studying rare species such as $^{56}Fe^+$. Triples $^{56}Fe^+$ starts triggering the SSD at 83 keV. The data from CHEMS' two highest energy steps (~192 and ~220 keV/e) contain a different kind of instrumental background and so are also excluded (see *Vandegrif et al.* [2012], paper 1, and Figure S2c in the supporting information). The heavy ion measurements displayed in Figure 1a are Triples pulse height analyzed (PHA) events, a subset of all ions measured by CHEMS. All PHA events are tagged with temporal, time of flight, energy, and directional information and are transmitted in addition to the counting rates of species groups for further detailed ion composition analyses. Full information on data characteristics, spatial sampling criteria, and intertelescope adjustments can be found in paper 1 (see also sections A and B in the supporting information). An M/Q adjustment we apply is crude but effective in aligning atomic ion species peaks from CHEMS' three telescopes at the appropriate mass per charge numbers (see section A2 in the paper 1 supporting information). CHEMS prelaunch calibrations were conducted for various species from H^+ to Kr^+, that is, from 1 to 83 amu/e. In this study's coincidence logic and energy channels, called BR5, CHEMS is sensitive to 83–167 keV/e ion responses at ~$0.5 \leq M < $~95 amu and ~$10.9 < M/Q < $~80 amu/e (see *Krimigis et al.* [2004] and section B in the supporting information). CHEMS' mass per charge resolution for heavy ions is much better than its mass resolution, as can be seen in Figure 1a. We improved our determination of the $^{56}M^+$ abundance by correcting the $^{56}Fe^+$ PHA counting rate for contributions from W^+ and O_2^+ straggling signals that extend into the 56 amu/e M/Q range (see Figure S2 in the supporting information). These straggling signals can extend into the $^{56}Fe^+$ M/Q collection range over a wider range of M values than ~$16 \leq M \leq$ ~19 amu, the mass range of the four W^+ components O^+, OH^+, H_2O^+, and H_3O^+, one atomic ion, and three molecular ions. The M distribution of all incident ions is broader for lower incident ion energy deposits as a result of interactions of the incident ion energy deposit and with electronic noise (probably Johnson-Nyquist noise) comparable to the magnitude of the incident ion's energy deposition. Each ion's energy deposition characteristics are unique, and somewhat different, especially the molecular ions. At high-energy deposition, electronic noise is less important and the M distribution is much narrower; compare, for example, M ranges in Figures S2(C) and S2(D), and either of these to, Figure S2c(A). Also, concerning a very different data analysis matter, we constructed a pseudospecies, W_{tail}^+, which is a dedicated M/Q analysis channel shown in Figure 1b which represents a significant portion of the W^+ straggling signals at higher M/Q. The various W^+ components might extinguish or dominate W^+ at different radial distances. This pseudospecies, W_{tail}^+, was created to sample, characterize, and monitor any possible temporal and/or spatial differences between the W^+ component species-related temporal/spatial straggling signal variations, only because W^+ represents four different species that originate from an unknown variety of different sources. This can alert one (see discussion at the end of section F) to any important differences between the principal W^+ peak variation at different radial locations and/or times that might result from differences in the straggling signals (see paper 1 and sections F and B in the supporting information). In this initial study, however, we have applied a single correction factor, independent of time and space, to test the veracity of an assumption of temporal/spatial independence. This signal correction process is similar to that detailed for W^+ underlying the $^{28}M^+$ and O_2^+ channels in paper 1, but
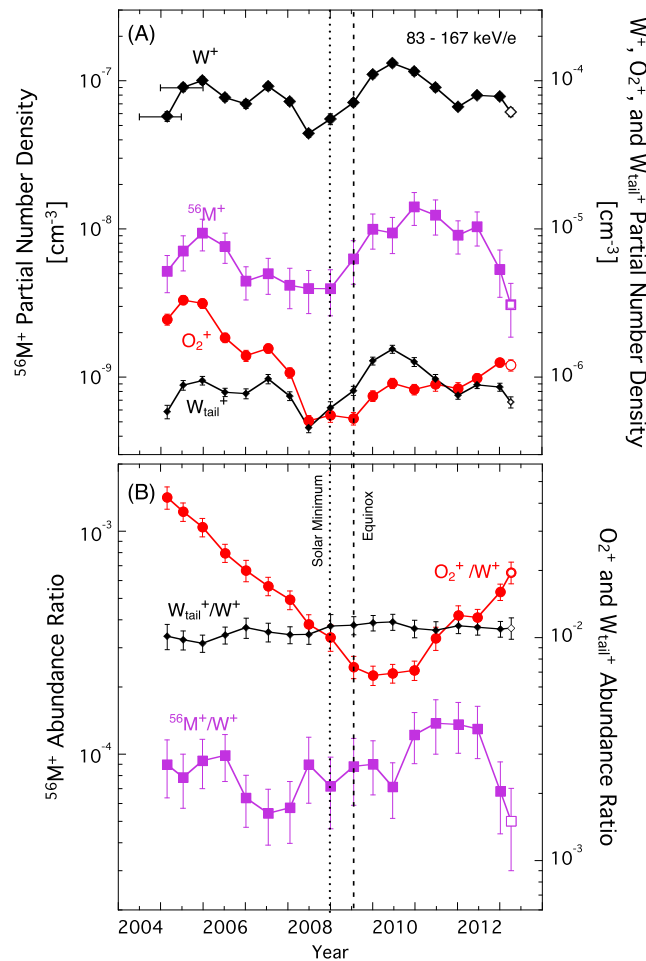
Figure 2. (a) Partial number densities, PND, and (b) abundance ratios of $^{56}M^+$, O_2^+, and W_{tail}^+ relative to W^+ are plotted versus time. Vertical axis scales for W^+, minor, and rare ion ratios are offset in both panels to facilitate easy comparison of relative abundance variations. Data are collected from mid-2004 to mid-2013 in 1 year interval moving averages stepped every half year. The moving averages are collected on strict calendar-year intervals and plotted at the mean time of the average. Uncertainties shown are standard error of the mean. Major tics on the time axis indicate the start and end of years. Open symbols for the final interval indicate that these values have a different radial sampling than the others (see text). Saturn equinox and solar minimum are indicated. W^+, O_2^+, and W_{tail}^+ are included for the purpose of comparison.

the correction for straggling tails in $^{56}M^+$ is small compared to that for $^{28}M^+$ and O_2^+. Because $^{56}M^+$ has low counts, only a single overall spillover adjustment one independent of time was applied (see section C in the supporting information for this paper and paper 1).

Our data set consists of 1 h average counting rates and PHAs (including all hours with and without species' PHA counts, except for those hours when no W^+ PHAs are measured), collected from day 2004–182 through day 2013–335 (YEAR-DOY, day of year), that are used to construct 1 h average differential intensities and partial number density, PND, values summed over 83–167 keV/e. Details of the CHEMS data selection criteria are given in paper 1 and its supporting information. Summarizing the selection process, we collect measurements overall portions of Cassini orbits inside of 20 Rs (or inside the magnetopause crossings which were determined from 2004–182 to 2007–349), at latitudes ≤ 45°, and $|Z_{szs}| <$ 5 Rs, and not affected by radiation belt backgrounds. As a result of the Cassini orbit, data have been obtained primarily at $L >$ ~4 to date. Of note, Cassini's orbits from mid-2013 until late-2014 cross Saturn's equatorial plane no closer than ~13 Rs and often near ~18–20 Rs from the planet (see section E in the supporting information and D. Seal, Cassini Mission Plan (JPL D-5564, Rev O, chg 1), PD 699-100, Revision O, Change 1, 2005, http://starbrite.jpl.nasa.gov/pds/viewMissionProfile.jsp? MISSION_NAME=cassini-huygens or http://caps.space.swri.edu/caps/

tourInfo/Documents/MP_O.pdf). These orbits prevent in situ sampling of the core of Saturn's ring current and inner magnetospheric ions until early 2015.

3. Observations and Analysis

Figure 1a is a M versus M/Q color spectrogram of Saturn's ~83–167 keV/e suprathermal heavy ions. Figure 1b is an M/Q histogram of the same data from 10 to 80 amu/e. The data are summed under our selection criteria (see section 2 above) overall intervals from day 182 of 2004 to day 335 of 2013; i.e., from SOI through all orbits in 2013. In order to place the rare ions in their proper context, Figure 1 indicates the primary heavy ion group, W^+, the minor heavy ions, C^+, N^+, $^{28}M^+$, and O_2^+, and the rare heavy ions $^{40}M^+$, $^{44}M^+$, and $^{56}M^+$. C^+, N^+, and W^+ have been analyzed elsewhere [*Mauk et al.*, 2009; *DiFabio*, 2012]. $^{40}M^+$ and $^{44}M^+$ will be discussed in a future paper. The $^{56}M^+$ peak (~56 amu/e is indicated by a small triangle above the top axis at 56 amu/e) is easily resolved in both Figures 1a and 1b. The Fe^{+1} peak is the highest M/Q peak observed

Figure 3. Running dipole L averages stepped every integer L value, with a 2 Rs window, are plotted versus L for (a) partial number densities, PND, and (b) abundance ratios of $^{56}M^+$, O_2^+, and W_{tail}^+ relative to W^+. The location of Rhea is noted in Figure 3a. The vertical axis scale of W^+ is offset in Figure 3a to facilitate easier comparison of the PNDs. In Figure 3a, two dashed gray curves have been added to represent two different offset levels of W^+, bounding statistical variations of $^{56}M^+$. Two gray straight line alternate extensions to these redrawn data curves at $L < 9$ are drawn for the purpose of comparison with the radial variation of $^{56}M^+$ at $L < 9$ (see text). The running averages are collected on strict integer L bounds and plotted at the mean distance of the average. Uncertainties shown are standard error of the mean. As a result of large uncertainties, several $^{56}M^+$ averages at $L \geq 14$ are considered upper limits and are shown paler and with distinct uncertainties. Open symbols at $L < 6$ identify data currently undersampled when compared to the other L intervals. Open symbols at $L > 19$ identify data which may be affected by proximity to the magnetopause.

persistently by CHEMS in long-term sums (see also Figures S1 and S12 in the supporting information). Note that there are no discernible ion signals at Fe^{+2} to Fe^{+5} charge state locations as indicated by the other small triangles from right to left above the top axis of Figure 1a between ~10 and 32 amu/e. As discussed in section 1, the lack of Fe peaks at the intermediate charge state locations of Fe^{+2} to Fe^{+5} indicates that Fe^{+1} is not a charge exchange product from higher charge state SEP, CME, or solar wind sources. As stated in above, because the CHEMS M/Q resolution at ~56 amu/e is only a few amu/e, we refer to the discovered species initially as $^{56}M^+$ to allow for the (unlikely) possibility that it could be some ion other than $^{56}Fe^+$.

3.1. Temporal Variations

Time variation of the $^{56}M^+$ PND, along with W^+, O_2^+, and W_{tail}^+ PNDs for comparison, are shown from mid-2004 through 2013 in Figure 2a. Abundance ratios relative to W^+, which we found useful in papers 1 and 2 for extracting the strong seasonal variations of O_2^+ and $^{28}M^+$ by removing common spatial/temporal population characteristics, are shown in Figure 2b. In order to present these data at as high a temporal resolution as possible, the data are collected using 1 year window moving averages stepped every half year. The arithmetic moving averages are collected on strict calendar-year bounds, including all 1 h samples, and plotted at the mean of the times of the samples. Uncertainties shown in Figures 2 and 3 are standard error of the mean. The last 1 year average is plotted at ~2013.3, not near ~2013.5, because of reduced near-equatorial orbital sampling at $R < 13$ Rs after

mid-2013 (see the discussion in paper 2 and section D in the supporting information). Average PND values may also be relatively reduced from ≈ 2008.5 to ≈ 2009.5, when Cassini was sampling the magnetosphere at slightly larger radial distances (see Figure S4). W_{tail}^+/W^+ shows little variation with time, arguing that the overall spillover contribution from the W^+ population to heavier ion M/Q channels remained relatively constant with time. Based on that constancy, a small background contribution from W^+ and O_2^+ was subtracted from $^{56}M^+$ as described above in section 2. All PND curves show general, mostly common (within $\pm$ ~0.5 year), large scale, likely magnetosphere-wide intensity variations.

Figure 2 shows that neither the $^{56}M^+$ PND nor $^{56}M^+/W^+$ show any variation related to solar minimum or Saturn equinox. The $^{56}M^+$ PND is somewhat variable, and, with larger fluctuations and uncertainties, its abundance ratio has a less well-determined temporal trend than O_2^+/W^+. The $^{56}M^+$ PND declines a bit until 2009.0 and then recovers quickly in ~1 year. By 2013.0, the $^{56}M^+$ PND returns to values comparable to or possibly lower than the starting values. Linear, exponential, and second-order polynomial regressions performed on the temporal profile of $^{56}M^+/W^+$ and a broad survey of the data indicate that no overall $^{56}M^+/W^+$ temporal trend, such as a seasonal variation, is supported by the current data (see Figures S6 and S12 in the supporting information).

3.2. Radial Variations

The radial variation of the heavy ion PNDs and abundance ratios are shown in Figures 3a and 3b, respectively. We use moving dipole L averages with 2 Rs data windows, stepped every integer L value, and plotted versus mean L. At $L \geq 6$, more than half of the L intervals have 1000 to 1300 samples and the rest have 836 to 1917 1 h samples. The two L averages at $L < 6$ have fewer than 800 one hour samples. At $L < 6$ and $L \geq 14$, the large uncertainties result from limited data and/or sampling (see section G in the supporting information); several of the $^{56}M^+$ averages at $L \geq 14$ considered to be upper limits are identified. The location of Rhea is shown for reference. Curve fits and regression values used for the following discussion can be found in section E of the supporting information. W^+, representing the dominant suprathermal ion populations, and O_2^+, representing the minor suprathermal ion populations, have prominent PND peaks at $L \sim 9$ typically with full width at half maximum of ~4 Rs. The exact radius of the suprathermal ion peaks depends on ion species and energy. Note that thermal energy ions do not exhibit such a local or overall density peak near $L \sim 9$ [see *Thomsen et al.*, 2010, Figure 7c]. That is, there are positive radial gradients inside and negative radial gradients outside the suprathermal ion peak at $L \sim 8$–9, consistent with significant suprathermal ion losses inside of $L \sim 8$–9, the nominal radial peak of Saturn's suprathermal ion properties [*Carbary et al.*, 2010; *Difabio*, 2012; *Sergis et al.*, 2007; paper 2]. Agreement with other studies' radial peaks suggests similar acceleration, transport, and loss processes over a wide range of species, energies, and radii. The W^+ PND data are redrawn at two representative levels (one central, one higher) as gray dashed curves through the $^{56}M^+$ PND points to show the overall similarity (within uncertainties) of the two species at $\sim 9 < L < \sim 18$. Exponential curves connect visual fits for the low L $^{56}M^+$ data to the redrawn W^+ curve peaks. But for the rings, all these ions would become trapped ions.

In contrast to the typical suprathermal ion species' radial dependence, the $^{56}M^+$ PND decreases roughly exponentially with increasing distance from Saturn. From $L \sim 5$ to $L \sim 9$, W^+ and O_2^+ PNDs increase by factors of ~7 and ~20, respectively, while the $^{56}M^+$ PND decreases with increasing L by a factor of ~4. The $^{56}M^+$ PND shows an approximate 2 order of magnitude decrease with increasing L overall. Two statistically insignificant $^{56}M^+$ PND local minima, at ~9 Rs and ~14 Rs, are present (see Figure S7 in the supporting information). The feature at $L \sim 9$ is near the orbit of Rhea and the peaks of the suprathermal ion PNDs, and at $L \sim 14$, there is nothing known for ions to interact with. The W_{tail}^+/W^+ upturn starting at $L \leq \sim 6$ continues inward, possibly indicating a radial variation between W^+ components. In section F of the supporting information, we demonstrate that even if the W_{tail}^+/W^+ variation is altered artificially by removing the increase at $L \leq 6$, and that alteration is then applied to O_2^+/W^+ and $^{56}M^+/W^+$, the two ratios still increase at $L < \sim 7$. Therefore, we conclude that the strong negative $^{56}M^+$ PND gradient at $L < \sim 6$ is not an artifact of the W^+ spillover adjustment.

4. Summary of Observations

These data show (a) $^{56}M^+$ is clearly observed as the highest M/Q ion peak discernible in the CHEMS M/Q histogram, (b) $^{56}M^+$ PND has a factor of ~50–100 decrease with increasing L, a negative radial gradient, at ~ 4–$5 < L < \sim 19$–20, (c) $^{56}M^+/W^+$ shows no clear long-term temporal variation, and (d) W^+ and O_2^+ have radial PND peaks at $L \sim 9$, typical for Saturn's suprathermal ion species in this energy range. Figure 1 shows no discernible ion peaks at M/Q greater than the $^{56}M^+$ peak. Therefore, the high mass water clusters observed by CDA are not detected by CHEMS. The positive ion PND radial gradients inside $L \sim 9$ most likely result from losses in the Enceladus torus [*Paranicas et al.*, 2008]. The negative $^{56}M^+$ PND radial gradient from $\sim 4 < L < \sim 9$ is somewhat stronger than the $^{56}M^+$ PND radial gradient at $L > 9$ (see Figure S7 in the supplementary information), suggesting that $^{56}M^+$ interaction with the Enceladus torus is complex. As a result of both less

Cassini orbital coverage and extant radiation belt backgrounds, insufficient suprathermal ion data has been obtained at $L < {\sim}4$ to determine any suprathermal heavy ion populations there.

The most likely candidate for $^{56}M^+$ is Fe^+ derived from IDPs gravitationally attracted to Saturn and impacting Saturn and/or its main rings. Alternatively or additionally, Fe^+ might derive primarily from Saturn's dark material in the main ring ices. Saturn's dark moon Phoebe, which spends most of its time outside Saturn's magnetosphere, is coated with and most likely coats the leading face of Iapetus with a dark material that is apparently found throughout the Saturn system and may be at least partially derived from cosmic material [*Cuzzi et al.*, 2009; *Clark et al.*, 2012]. Whatever the source material, we conclude that $^{56}M^+$ is the atomic ion Fe^+ and call it Fe^+ hereafter.

5. Discussion of Fe/Fe⁺ Production and Dissemination Scenarios

Two likely Fe^+ sources are Saturn's ionosphere and/or the portion of the main rings directly accessible to the magnetosphere, the A and outer B rings. Both locations may be simultaneously producing Fe^+. Suprathermal Fe^+ PND has a roughly overall exponential decrease from ${\sim}5$ to ${\sim}20$ Rs. Comparison of redrawn W^+ PND traces to Fe^+ PND data demonstrates an overall similarity (within uncertainties) $L > {\sim}9$. At $L < {\sim}9$ they are dramatically different. The distinct radial dependence of the Fe^+ PND is likely related to one or a combination of two properties of Fe^+: (a) its escape scenario from its source location and (b) its scattering and loss interactions with the equatorial Enceladus torus neutral populations. We note that the two sources for Fe^+ suggested above are different from those suggested for the other suprathermal ions, except for the O_2^+ population which evolves from ring ice.

We consider the possibilities that the observed suprathermal Fe^+ either (a) is generated in the inner magnetosphere at thermal energies in Saturn's ionosphere or in the main rings, spread to the outer magnetosphere, and accelerated in transit back toward Saturn, similar to the manner in which ring origin O_2^+ is accelerated to suprathermal energies; or (b) arises directly from a source of suprathermal Fe^+ flowing out of Saturn's high-latitude auroral region and seeding the $L > {\sim}6$ magnetosphere. Unlike W^+ and O_2^+ though, Fe^+ does not exhibit significant losses at $L < 9$. Below, we discuss scenarios for production, escape, and dissemination of thermal energy Fe^+ from two alternate sources, Saturn's ionosphere and its rings, and its acceleration to suprathermal energies, considering both the positive and negative aspects of each scenario. Production and outflow from Saturn's ionosphere are separated into two different modes: thermal Jeans escape which is representative of possible escape from the ionosphere at subauroral latitudes, that is, at latitudes below the auroral region from 0° to ${\sim}70°$ latitude, and dynamic auroral outflow.

5.1. Fe⁺ From the Subauroral Ionosphere
5.1.1. Ionospheric Fe⁺ Production

The first possible source of Fe^+ that we address is meteoric metal layers near the mesosphere-ionosphere boundary at Saturn, similar to the well characterized and reasonably understood ionospheric metal layers at Earth. Such meteoric origin layers have not as yet been definitively observed at Saturn or Jupiter, but early analyses of Cassini data showing likely low-ionospheric layered structure at Saturn is encouraging [*Molina-Cuberos et al.*, 2008; *Nagy et al.*, 2009]. Using Mg as a representative meteoric metal (other meteoric species include Na, Fe, C, and Si), *Moses and Bass* [2000] modeled meteoric layers at Saturn, addressing, among other effects, the recently documented "ring rain," i.e., water influx from the main rings to Saturn's midlatitude atmosphere [*O'Donoghue et al.*, 2013]. Given that meteoric layers exist at Saturn, ionospheric mixing, such as that at Earth (see e.g., *Grebowsky and Aikin* [2002]), can spread some metal layer ions throughout the ionosphere.

Meteoric ablation is the most probable source of atomic iron (Fe and Fe^+) in Saturn's ionosphere. Meteoroids enter the atmosphere with a narrow velocity range (35.5–42.5 km s^{-1}), and their ablation should peak around the 7 μbar level (800 km altitude above the 1 bar level) [*Moses and Bass*, 2000]. Because of the large atmospheric scale height (${\sim}50$ km) in this part of the atmosphere, ablation will extend over a large vertical distance (${\sim}200$ km) compared with the Earth, where the small scale height (${\sim}4$ km) restricts ablation to a height range of ${\sim}30$ km [*Vondrak et al.*, 2008]. Since the meteoroid entry velocity into Saturn's atmosphere is relatively high, around 20% of the ablating Fe will ionize through hyperthermal collisions with H_2 [*Vondrak*

et al., 2008]. Ionization will also occur through charge exchange with the dominant hydrocarbon ion $C_3H_5^+$, which has a concentration of ~1000 cm^{-3} at 800 km [*Moses and Bass*, 2000]:

$$Fe + C_3H_5^+ \rightarrow Fe^+ + C_3H_5. \tag{1}$$
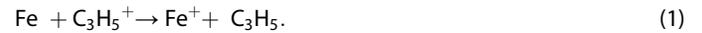
Langevin theory can be used to estimate a temperature-independent rate coefficient $k_1 = 1.4 \times 10^9$ cm^3 s^{-1} for reaction (1). Note that photoionization does not compete with reaction (1) in the lower ionosphere (see below). Neutralization will mostly occur through cluster formation,

$$Fe^+ + C_2H_6(+H_2) \rightarrow Fe^+.C_2H_6, \tag{2}$$

$$Fe^+ + C_2H_2(+H_2) \rightarrow Fe^+.C_2H_2, \tag{3}$$
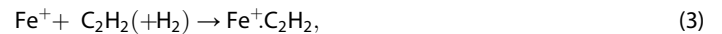
followed by dissociative recombination (DR) with electrons:

$$Fe^+.X + e^- \rightarrow Fe + X \ (X = C_2H_6, C_2H_2 \text{ etc.}). \tag{4}$$
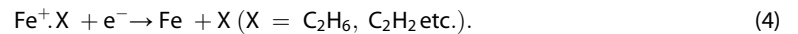
The rate coefficients for reactions (2) and (3) have been measured at 294 K [*Baranov et al.*, 1997]. Assuming a T^{-2} dependence typical of reactions of this type [*Vondrak et al.*, 2006], then the rate coefficients for reactions (2) and (3) are $k_2 = 5.7 \times 10^{-27}$ cm^6 molecule^{-2} s^{-1} and $k_3 = 6.6 \times 10^{-27}$ cm^6 molecule^{-2} s^{-1} at 140 K, respectively, which is a representative temperature at 800 K [*Moses and Bass*, 2000]. Note that although CH_4 and H_2 are much more abundant in Saturn's lower ionosphere, these species bind very weakly with Fe^+ and their clustering reactions are too slow to be of significance [*Baranov et al.*, 1997]. For reaction (4) we assume a typical DR rate coefficient of 4×10^{-7} cm^3 s^{-1} [*Florescu-Mitchell and Mitchell*, 2006].

The reaction sequence (2)-(4) would result in Fe^+ being converted overwhelmingly to Fe. However, there is a significant concentration of atomic H around 800 km [*Moses and Bass*, 2000], which should compete effectively with DR to prevent neutralization:

$$Fe^+.X + H \rightarrow Fe^+.H + X, \tag{5}$$

$$Fe^+.H + H \rightarrow Fe^+ + H_2. \tag{6}$$

To test the viability of reactions (5) and (6), we performed electronic structure calculations using the Gaussian 09 suite of programs [*Frisch et al.*, 2009]. At the B3LYP/6-311 + G(2d,p) level of theory, the relevant cluster binding energies of Fe^+ with C_2H_6 and C_2H_2 are 59 and 95 kJ mol^{-1}, respectively, whereas the Fe^+H bond energy is 232 kJ mol^{-1}. Reactions (5) and (6) are therefore highly exothermic (by 150–190 kJ mol^{-1}), and we assume them to be fast ($k_5 = k_6 = 4 \times 10^{-10}$ cm^3 molecule^{-1} s^{-1}).

The ratio of Fe^+ to Fe can then be estimated from the steady state expression

$$\frac{[Fe^+]}{[Fe]} = \frac{k_1 [C_3H_5^+]}{(k_2 [C_2H_6][H_2] + k_3 [C_2H_2][H_2]) \left(\frac{k_4 [e^-]}{k_4 [e^-] + k_5 [H]} \right)}. \tag{7}$$

Using the concentrations from the model of *Moses and Bass* [2000], the Fe^+/Fe varies from 10% at 800 km to essentially 100% Fe^+ at altitudes above 900 km.

Based on a 1-D model of Mg^+ in Saturn's ionosphere [*Moses and Bass*, 2000], the ablation flux of Fe/Fe^+ should be ~10^5 cm^{-2} s^{-1} to be consistent with the inferred influx of extraplanetary O required to model the observed CO and H_2O. Assuming a lifetime of 10 days before removal on meteoric smoke particles, then the concentration of Fe^+ in the 900–1000 km region of Saturn's atmosphere would be around 10^4 cm^{-3}. In comparison, a 3-D model of Fe/Fe^+ in the terrestrial atmosphere requires an ablation flux of ~10^4 cm^{-2} s^{-1} to model the observed Fe and Fe^+ layers [*Feng et al.*, 2013]. Interestingly, Earth's meteoric Fe^+ layer concentration is also around 10^4 cm^{-3}. It will be interesting to compare the Fe^+ PNDs in Earth's magnetosphere to those at Saturn once characterized it with an instrument, the Geotail supra-thermal ion composition spectrometer, with energy range comparable to Cassini/CHarge-Energy-Mass ion Spectrometer.

5.1.2. Ionospheric Fe^+ Escape

A difficulty for the subauroral ionosphere in providing a source of Fe^+ beyond the rings is the very large escape velocity required. The thermal Jeans escape flux of a heavy species such as Fe^+ is essentially zero. Reaction (4), where around 7 eV of energy would go into kinetic energy of the products, will produce hot Fe atoms. However, with a velocity of only ~ 3 km s^{-1}, they would not travel more than 500 km from the planet

under collisionless conditions (which is of course not the case at 1000 km). It therefore appears, at first, difficult for a supply of thermal-escape Fe/Fe$^+$ from the lower ionosphere to be the source of the suprathermal Fe$^+$ observed in Saturn's magnetosphere. Because a number of other processes at Saturn are similar to processes in Earth's atmosphere, in analogy to Earth's magnetosphere, we note that there are several dynamic escape processes for ionospheric ions which we call collectively ionospheric outflow.

Dynamic escape from the ionosphere may proceed either as a process similar to that connecting thunderstorms in Saturn's atmosphere to main ring spoke regions through field-aligned electron currents [*Jones et al.*, 2006] or active high-latitude processes similar to Earth's dayside cusp/cleft region, polar wind, and/or the nightside auroral oval which likely result in the ~30 keV to ~200 keV ion conics accompanied by ~20 keV to ~1 MeV electron beams measured at Saturn [*Mitchell et al.*, 2009a]. The Saturn ion conics at ~10 < L < ~50 are usually seen in conjunction with auroral activity and enhanced broadband electromagnetic noise in the 10 Hz to few kHz frequency range. As observed, Saturn's ion conics are almost exclusively light ions (including a combination of H$^+$, H$_2^+$, and/or H$_3^+$), but with hints of heavy ions (generically identified as O$^+$, as noted above). Ion conics have been mapped back to active auroral regions in Saturn's ionosphere by *Badman et al.* [2012] and are presumed to result from ionospheric outflow processes. *Badman et al.* [2012] report, in addition to upward beams of 100–360 keV light ions and 200–1000 keV electrons, the presence of ~250–600 keV upward directed heavy ions identified as having masses ≥16 amu, generically called O$^+$, but a heavy ion composition that possibly includes Fe$^+$. The actual relative heavy to light ion abundance ratio is not known. These ion bursts were observed in Saturn's high-latitude dayside at ~1230–1330 local time (LT) on field lines mapping back to Saturn's cusp region [*Badman*, 2012]. The narrow beam-like ion distributions and their correspondence with broadband electromagnetic wave enhancements are the same as for the ion conics identified by *Mitchell et al.* [2009a]. *Lockwood et al.* [1985a, 1985b] found that dayside outflowing ions at Earth's cusp were spread spatially by gravity so that heavier/slower ions fell to lower latitudes (or the equator) sooner than lighter/faster ions; and in a review of Earth's polar wind observations, *Yau et al.* [2007] argued that Earth's polar wind outflow velocities are also mass differentiated (see their Figure 4). However, because the escape speeds are higher at Saturn, the species' outflows are much less likely to be mass differentiated at Saturn than at Earth. Nevertheless, Fe$^+$ might escape with the outflowing several hundred keV light and heavy ions observed associated with Saturn's cusp region. The outflowing ion conics were measured at magnetospheric locations at a wide range of local times from ~10 < L < 20 and at up to ≥28 Rs in the tailward direction. Any ionospheric Fe$^+$ escape at lower latitudes to the rings with subsequent escape to the outer magnetosphere will experience the same challenges as Fe$^+$ produced in the rings from meteoric debris and/or Saturn's dark material. This process is discussed below in section 5.2.2.

At Saturn, as at Earth, outflowing ions on closed, nearly dipolar field lines can be scattered off the initial L shell. Logically, if this did not happen, say, at Earth, for example, all field-aligned beam products from auroral regions on dipole-like field lines would likely travel to the opposite hemisphere and be reabsorbed into the ionosphere within a bounce period or so. As a result, ionospheric ions from closed fields would not dominate magnetospheric populations during disturbed intervals (as they are know to do), and those ionospheric ions on open polar field lines would escape the system. One way field-aligned particles on initially dipole-like fields can be lost by scattering in the more disturbed, high-beta magnetospheric current sheet magnetic field. *Bunce et al.* [2008] model the ring current perturbation of Saturn's planetary (dipolar) magnetic field as present from 7.5 to 18.0 Rs. *Arridge et al.* [2008] and *Kellett et al.* [2009] present magnetic field data showing various levels of enhanced turbulence near the equatorial current sheet/magnetodisk in the > ~9 Rs equatorial region. The *Arridge et al.* study only used perturbation fields greater than the planetary field and focused on > ~15 Rs. However, magnetic fields often observed with a slightly stronger planetary field component with smaller variability closer to the planet might easily disrupt field-aligned particle motion. Additionally, the equatorial plane contains much neutral icy material (scattering or absorption) and both positively (at ≥ ~7 Rs) and negatively (at ≤ ~8 Rs) charged material (see Figure 1 in *Kempf et al.* [2006] and references therein). This charged material might also present a level of electrostatic perturbation in addition to the electrodynamic magnetic field perturbations.

5.2. Fe$^+$ From the Main Rings
5.2.1. Main Ring Fe$^+$ Production
Production of Fe$^+$ from iron compounds in the A and outer B rings would be affected by chemical processes in Saturn system ices and facilitated by photolysis during insolation and/or radiolysis from MeV energy

radiation belt and/or GCR splash particles striking the A ring and outer B ring [*Chenette et al.*, 1980; *Paranicas et al.*, 2008; *Kollmann*, 2012]. There are at least two originating sources for iron compounds to be found in the rings, either from infalling cosmic material which should always be impacting and embedding itself in the rings, or from the Saturn system's dark material transported to the rings in or on ice grains which pervade the magnetosphere. As iron compounds on the surfaces of meteoric dust such as hematite and magnetite interact with the ice, the compounds may reduce toward FeO. Alternatively, hematite and/or magnetite in A ring material may continually be dissociated radiologically by the ever present radiation belt particles.

The A and outer B rings are a possible source of the Fe^+ observed at $L > 4$. As noted in section 1, there is strong spectroscopic evidence that the icy particles in the rings probably contain contaminant-level concentrations of iron in different forms, either from direct implantation by cosmic material gravitationally drawn to Saturn or from the dark material that has been suggested as the UV absorber in the main rings. There are two ways the Fe/Fe^+ could be ejected into the gas phase. The simplest mechanism is through collisions of meteoroids with main ring particles, which both partially ablate the meteoroid and release Fe contaminants trapped in the ice. This can probably occur in any of the main rings. A second mechanism for producing Fe/Fe^+ is sputtering by radiation belt protons (electrons) whose intensities at ~2.5 and 38.5 (~11.8) MeV peak locally near and extend into the outer edge of the A ring [*Kollmann et al.*, 2011]. Sputtering by collisions with low-energy ions such as the O^+ and O_2^+ reported with densities of around 2–4 cm^{-3} at thermal energies by *Tokar et al.* [2005] over the main rings may also produce Fe/Fe^+. In a recent laboratory study [*Frankland and Plane*, 2015], Fe atoms were deposited into an ice film in an ultrahigh vacuum chamber. Sputtering with Ar^+ ions with energies of only 600 eV ejected Fe (and a small amount of $Fe(OH)_2$) from the ice with a yield around 10% in the laboratory, demonstrating that ion sputtering from less-than-radiation-belt-energy ions may be another source of Fe/Fe^+ in the vicinity of the rings. It has also been postulated that energetic, ~100 keV, electron bombardment of the rings can occur through magnetic connections to lightning in thunderstorms [*Jones et al.*, 2006].

Once in the gas phase, Fe^+ will be produced by photoionization

$$Fe + h\nu \rightarrow Fe^+ + e^-. \tag{8}$$

The photoionization rate at Saturn for reaction (8) should be around $J_8 = 5 \times 10^{-8} \, s^{-1}$, based on the calculated photoionization cross section [*Bautista et al.*, 1998]. In contrast to the lower ionosphere (see above), the density of ions around the rings with which Fe could charge transfer is too low to compete with photoionization. Similarly, formation of Fe^+-cluster ions will be extremely slow, so that Fe^+ will be converted to Fe by dielectronic/radiative recombination:

$$Fe^+ + e^- \rightarrow Fe + h\nu. \tag{9}$$

At a typical temperature of 70 K [*Tokar et al.*, 2005], $k_9 = 1.4 \times 10^{-11} \, cm^3 \, s^{-1}$ [*Bautista et al.*, 1998]. At steady state,

$$\frac{[Fe^+]}{[Fe]} = \frac{J_8}{k_9[e^-]}. \tag{10}$$

Around the A and B rings, $[e^-] \sim 4 \, cm^{-3}$ [*Tokar et al.*, 2005], so $[Fe^+]/[Fe] = \sim 10^3$. This means that once Fe has been sputtered into the gas phase, it will overwhelmingly be converted to Fe^+, even though the *e*-folding time to ionize Fe is around 200 days.

5.2.2. Main Ring Fe^+ Escape

Thermal energy Fe^+ above the rings, from whatever source, encounters a difficulty in supplying suprathermal energy Fe^+ directly to ~4 *Rs*, that is, we know of no acceleration process at equatorial ~2–4 *Rs* that could accelerate thermal ions above the rings to suprathermal energies at ~4 *Rs*. Therefore, we rule out direct supply of suprathermal Fe^+ from the ring region to ~4 *Rs*. If ionospheric escape of Fe^+ directly to the main rings is somehow possible, escape from the rings is limited. Inside of ~1.8 *Rs*, which is the approximate radius where Keplerian and corotation velocities are equal, *Luhmann et al.* [2006] and *Tseng et al.* [2010] found that particles were unable to escape to the magnetosphere. However, outside 1.8 *Rs*, particles were able to escape. A wider surface area of Saturn is on dipole magnetic field lines connected to the D, C, and inner B rings inside ~1.8 *Rs*, with dipole connection latitudes of ~18° to ~42°, than on field lines connected to the outer B and A rings outside ~1.8 *Rs*, with dipole connection latitudes between ~42° and ~49° (see Figure S14 in the supporting information). Mixing and radial redistribution of ring materials in the tumbling B ring might provide scenarios for additional ionospheric Fe^+ to be present above the outer B ring. Nevertheless, a

small thermal energy Fe^+ scattering cross section (as implied by the ~30 keV Fe^+-on-O cross-section variation, see section 5.4) would likely limit its ability to escape from the rings as easily as O_2^+. However, if the thermal Fe^+ scattering cross section is not too small and if Fe^+ is not extinguished by the ring's O_2/O_2^+ atmosphere/ionosphere, thermal Fe^+ could scatter via multiple collisions to the outer magnetosphere as thermal energy ring origin O_2^+ is thought to do [*Tseng et al.*, 2010], but this is probably unlikely for the reasons mentioned above. If it is found in subsequent research and modeling that the thermal energy Fe^+ scattering cross section is not small, then escape of thermal Fe^+ from over the rings remains a naturally expected seed population for any suprathermal Fe^+ accelerated in Saturn's ~15–20 Rs recurrent acceleration regions followed by inward radial diffusion while conserving the first and second adiabatic invariants to Saturn's $L < $ ~8–9 magnetosphere.

5.3. Fe^+ From Saturn's Auroral and Polar Region Ionosphere

Observed outflowing suprathermal light and heavy ion beams and conics travel from the aurorae to Saturn's equatorial, middle magnetosphere along stretched dipole-like field lines throughout all local times at $L < $ ~20 [*Badman et al.*, 2012; *Mitchell et al.*, 2009a; *Bunce et al.*, 2008]. Light (heavy) ions from the auroral acceleration regions have initial escape energies less than or equal to ~200 keV (~600 keV). As also noted in section 1, the radius of equatorial access might be as close as $L \sim 6.5$ at times from Saturn's southern auroral region. That is, some heavy ions in CHEMS energy range may be directly introduced into the equatorial region by field-aligned auroral outflow. Ions in the beams and conics that are initially on or scattered onto L shell field lines in the ~6.5 $< L < $ ~10 closed field region and not neutralized will mirror at higher latitudes, and as the ions in scenario 1, gradient and curvature drift in the rotating dipole-like magnetic field structure. Presently, this is only a heuristic model, with no theoretical modeling yet performed. It is anticipated that such modeling of both the similarities and the differences between Fe^+ production processes at Saturn and possibly similar Fe^+ production processes at Earth will be engaged in by the scientific community.

5.4. Fe^+ Return to the Inner Magnetosphere

Two qualitatively different initial scenarios for Fe^+ return to the $L < $ ~9 magnetosphere have been considered (1) thermal energy Fe^+ from the rings and/or the ionosphere are scattered into the ~15–20 Rs outer magnetosphere where they attain higher energies in extant recurrent acceleration regions and (2) hundred keV energy, high-altitude ionospheric ions are directly introduced at $L \geq$ ~10 into the middle magnetosphere, flowing outward from near-auroral sources and scattering in the near-equatorial plasma sheet contributing to the near-equatorial suprathermal ion population. Both initial scenarios are followed by energization by inward radial diffusion at $L > 4$ while conserving the first and second adiabatic invariants. By $L < $ ~4, most or all such ions are likely extinguished by interactions with neutral populations. While our focus is on Saturn in this paper, we note that Titan, with a thick atmosphere, is also a possible source of escaping meteoric metal ions [*Molina-Cuberos et al.*, 2001]. Titan might easily seed thermal energy Fe^+ at ~20 Rs, ions which would then be subject to scenario 1.

In support of scenario (1), we use offset W^+ curves in Figure 3a to show graphically that, within measurement uncertainties, Fe^+ and W^+ have comparable radial dependences at $L > $ ~9. It is documented that thermal to low-energy ions in Saturn's ~15–20 Rs magnetosphere are routinely accelerated to hundred keV energies by localized recurrent acceleration events which spread quickly inward to ~7 Rs [*Mitchell et al.*, 2005, 2009b]. An example ascribed to scenario (1), the most likely explanation for the suprathermal O_2^+ population is that its dominant component originates from photolysis of ring; and therefore, its intensity varies seasonally (see paper 1). Thermal energy O_2^+ spreads to the outer magnetosphere and is accelerated by either one or a combination of two processes, conservation of the first two adiabatic invariants during inward radial diffusion, and/or, sporadic acceleration in the recurrent acceleration regions (see paper 1 and references therein). Because Fe^+ shows no seasonal variation, it is likely that its origin does not depend on photolysis. The acceleration of an external Fe^+ source would undergo a similar process. That is, as mentioned in section 1 and discussed in section K of the supporting information, there might a possibility that Fe^+ arises from an external source, the ACRs or ISPUIs. The greatest problem with an external source possibility is that there are no consistent, clear, repeatable observations of purported Fe^+ from either of those populations at any energy to our knowledge. The one clear, repeated report of Fe^+ is from Earth's inner radiation belts [*Mazur et al.*, 1999, 2000, 2008]. As mentioned in section 1, we have measured suprathermal Fe^+ in Earth's magnetospheric
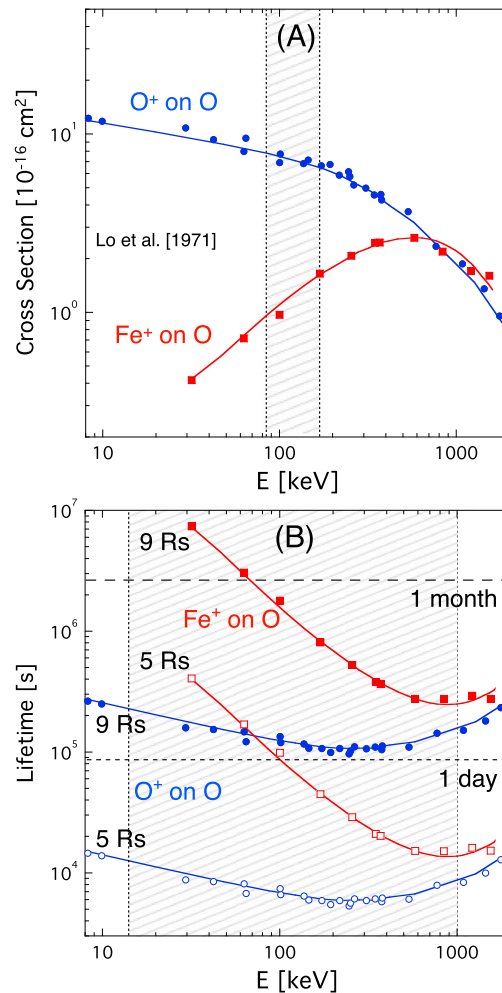
Figure 4. O^+ and Fe^+ electron capture cross sections and lifetimes at 9 and 5 Rs in the ~8–2000 keV range. (a) Experimentally determined electron captures cross-section data, and their fits plotted by *Lo et al.* [1971] are digitized from their Figures 4, 5, and 13 for O^+ and Fe^+ incident on O. O and O^+ are, respectively, used to represent the water group neutral (W) and ionized (W^+) component species, OH^+, H_2O^+, and H_3O^+, in our lifetime calculations that use the neutral atom model of *Cassidy and Johnson* [2010]. The shaded portion of Figure 4a denotes this study's energy range, 83–167 keV. (b) Lifetimes are shown for data in the shaded portion of Figure 4a. The shaded portion of Figure 4b denotes the range of energies that can be mapped to or from this study's energy range between 9 and 5 Rs. Intervals of 1 day and 1 month are shown.

environs at $R >= 9 R_E$. We are in the process of calculating the necessary abundance parameters in order to study this population at Earth. This suprathermal population might be accelerated and incorporated into Earth's trapped radiation belts, as are some SEP ions [*Mason et al.*, 1996].

In support of scenario (2), we note that up to ~200 keV light and up to ~600 keV heavy ions escape from the auroral acceleration regions. The radius of equatorial access from the auroral regions might be as close as $L \sim 6.5$ at times from Saturn's southern auroral region but is more likely in the ~9–14 auroral region. Some outflowing suprathermal heavy ions in CHEMS energy range may be directly introduced into the equatorial region. Ions can be scattered onto L shell field lines in the ~6.5 < L < ~10 closed field region, and those not neutralized will mirror at higher latitudes, and as the ions in scenario 1, gradient and curvature drift in the magnetic field structure. Scenarios 1 and 2 can operate simultaneously. All ions can gain energy by inward radial diffusion while conserving the first and second adiabatic invariants [*Schardt and Goertz*, 1983; *Mauk et al.*, 2009; *Kollmann et al.*, 2011]. But for the rings, these ions would become trapped.

Inside $L \sim 9$, only suprathermal Fe^+ has a PND radial profile that continues to increase with decreasing L. The decline of the major ion species in that region is thought to result from charge exchange loss with an increasingly dense neutral torus as they diffuse inward from the middle magnetosphere [*Paranicas et al.*, 2008]. A difference in loss rates could explain the different behavior of Fe^+. The charge exchange lifetime τ depends on the electron capture cross section σ, the neutral density n, and relative collision velocity v according to $\tau = (\sigma n v)^{-1}$. Figure 4a presents measured charge exchange cross sections of O^+ and Fe^+ incident on neutral O from *Lo et al.* [1971]. $\sigma(O^+$-on-O), commonly used in interpretation of energetic neutral ion

data [*Lindsay and Stebbings*, 2005], and $\sigma(Fe^+$-on-O) are the definitive cross sections for these species in the keV to MeV energy range (see also section 1 in the supporting information). Although the W^+ we measure contains the other water group species, cross sections are not available for them, and we use O^+ as a representative species. Over the 83–167 keV energy range used in this paper, the Fe^+ cross section is considerably smaller than that of O^+, varying from a factor of ~8 smaller at the lower energy to ~4 times smaller at the higher energy. In Figure 4b, we use neutral densities from the model of *Cassidy and Johnson* [2010] to calculate charge exchange lifetimes at 5 Rs and 9 Rs. Once again we treat their total density, which is made up of O, OH, and H_2O, as all being O for the purpose of these calculations. The Fe^+ lifetime varies from a few weeks at 9 Rs to about a day at 5 Rs. This is a factor of ~14 longer than O^+ at 83 keV decreasing to a factor of ~7 longer at 167 keV. The larger difference in lifetimes than cross sections is due to the lower speed of Fe^+

at the same kinetic energy. The longer Fe^+ lifetime at least qualitatively explains the persistence of suprathermal Fe^+ into 5 Rs. The W^+ PND begin to decrease inside of $L \sim 9$ at which distance its lifetime is a little over a day. The Fe^+ lifetime is only slightly less than that at 5 Rs. Additionally, if the observed suprathermal ions are gaining energy during inward radial diffusion, then the increasing lifetime of Fe^+ at lower energies gives it another advantage over W^+. Conservation of the first adiabatic invariant implies a variation of an ion's energy proportional to |B| or to r^{-3} in this nearly dipolar region. The shaded portion of Figure 4b denotes the approximate full range of energies that this study's energy range can be mapped to or from between 9 and 5 Rs by inward radial diffusion. Ions with energy of 167 keV at 5 Rs would have had an energy of 29 keV at 9 Rs. The lifetime of 29 keV Fe^+ at 9 Rs is about 3 months, while that of 29 keV O^+ is only about 2 days. Detailed transport modeling is required to quantitatively verify these arguments and is beyond the scope of this paper.

6. Summary

Thermal energy Fe^+ most likely originates either in Saturn's ionosphere or in the A and outer B rings. If Fe^+ originates in Saturn's ionosphere, its most likely escape routes are from the cusp/cleft region near the auroral oval and/or the auroral oval. Current observations show that heavy ions of unknown composition, some of which may be Fe^+, escape at suprathermal energies from near-auroral regions. When this occurs, little to no further acceleration may be needed to reach the energies and locations of the CHEMS observations herein at $L > \sim 6.5$, a distance accessible from Saturn's southern auroral oval. However, $L \sim 9–15$ is much more likely. At those radii, there are ions, neutrals, and E ring particles to scatter from or just to diffuse into lower L values. There is likely a wider range of energies than currently observed at which auroral ions flow out and the entire ensemble may appear equatorially at $\sim 9–15$. As for thermal ion escape from the ionosphere, we have shown above that Jeans escape flux of a thermal energy heavy species such as Fe^+ is essentially zero from the lower ionosphere. If thermal energy Fe^+ originates in the A and outer B rings, it might be scattered into the outer magnetosphere in a manner similar to that of ring origin O_2^+, but, to our knowledge, scattering characteristics of thermal energy Fe^+ in the ring atmosphere/ionosphere are currently incompletely determined. Fe^+ likely has a smaller scattering cross section than O_2^+, so the scattering process that transports O_2^+ away from the rings may be inefficient for Fe^+. In cases other than escape from the cleft or auroral oval at hundred keV energies, escaped Fe^+ needs to access the recurrent acceleration regions in the outer equatorial magnetosphere where it can be accelerated to keV energies. Thermal energy Fe^+ present in the outer magnetosphere is likely to be accelerated in the recurrent acceleration regions and return to the inner magnetosphere at suprathermal energies. Any or all of these escape routes and scenarios may exist and be active simultaneously.

Meteoric layers in planetary atmospheres/ionospheres exist. Escaping ionospheric outflow at the energies observed near ~ 600 keV at Saturn could extract Fe^+ from the low to middle ionosphere at the same time it obviously extracts ~ 600 keV heavy ions observed in the outflowing ion conics reported by *Badman et al.* [2012] from higher-latitude auroral regions. After all processes have been modeled and investigated thoroughly, this last scenario may provide the simplest, straightforward explanation of the observed suprathermal Fe^+ at ≥ 4 Rs. It remains that $\sim 83–167$ keV Fe^+ has been clearly observed throughout Saturn's magnetosphere at near-equatorial distances less than ~ 20 Rs with a partial number density maximum at $L \sim 4–5$, the lowest radial distances sampled.

References

Anders, E., and N. Grevesse (1989), Abundances of the elements: Meteoritic and solar, *Geochim. Cosmochim. Acta.*, *53*, 197–214, doi:10.1016/0016-7037(89)90286-X.

Arridge, C. S., C. T. Russell, K. K. Khurana, N. Achilleos, S. W. H. Cowley, M. K. Dougherty, D. J. Southwood, and E. J. Bunce (2008), Saturn's magnetodisc current sheet, *J. Geophys. Res.*, *113*, A04214, doi:10.1029/2007JA012540.

Badman, S. V. (2012), Comparative cusp processes, abstract ST14-A016 at the Asian Oceania Geosciences Society (AOGS), Singapore, August.

Badman, S. V., S. W. H. Cowley, J. -C. Gérard, and D. Grodent (2006), A statistical analysis of the location and width of Saturn's southern auroras, *Ann. Geophys.*, *24*, 3533–3545, doi:10.5194/angeo-24-3533-2006.

Badman, S. V., et al. (2012), Cassini observations of ion and electron beams at Saturn and their relationship to infrared auroral arcs, *J. Geophys. Res.*, *117*, A01211, doi:10.1029/2011JA017222.

Badman, S. V., et al. (2014), Saturn's auroral morphology and field-aligned currents during a solar wind compression, *Icarus*, doi:10.1016/j.icarus.2014.11.014, in press.

Baranov, V., H. Becker, and D. K. Bohme (1997), Intrinsic coordination properties of iron: Gas-phase ligation of ground-state Fe^+ with alkanes, alkenes, and alkynes and intramolecular interligand interactions mediated by Fe^+, *J. Phys. Chem. A*, 101(28), 5137–5147.

Bautista, M. A., P. Romano, and A. K. Pradhan (1998), Resonance-averaged photoionization cross sections for astrophysical models, *Astrophys. J. Suppl. Ser.*, 118(1), 259–265.

Bridges, J. C., M. J. Burchell, H. C. Changela, N. J. Foster, J. A. Cre, J. D. Carpenter, S. J. Gurman, I. A. Franchi, and H. Busemann (2010), Iron oxides in comet 81P/Wild 2, *Meteorit. Planet. Sci.*, 45, 55–72, doi:10.1111/j.1945-5100.2009.01005.x.

Bunce, E. J., C. S. Arridge, S. W. H. Cowley, and M. K. Dougherty (2008), Magnetic field structure of Saturn's dayside magnetosphere and its mapping to the ionosphere: Results from ring current modeling, *J. Geophys. Res.*, 113, A02207, doi:10.1029/2007JA012538.

Carbary, J. F. (2012), The morphology of Saturn's ultraviolet aurora, *J. Geophys. Res.*, 117, A06210, doi:10.1029/2012JA017670.

Carbary, J. F., N. Achilleos, and C. S. Arridge (2010), Statistical ring current of Saturn, *J. Geophys. Res.*, 117, A06223, doi:10.1029/2011JA017472.

Carter, L. N., and J. M. Forbes (1999), Global transport and localized layering of metallic ions in the upper atmosphere, *Ann. Geophys.*, 17(2), 190–209, doi:10.1007/s00585-999-0190-6.

Cassidy, T. A., and R. E. Johnson (2010), Collisional spreading of Enceladus' neutral cloud, *Icarus*, 209, 696–703, doi:10.1016/j.icarus.2010.04.010.

Chandler, M. O., J. H. Waite Jr., and T. E. Moore (1991), Observations of polar ion outflows, *J. Geophys. Res.*, 96(A2), 1421–1428, doi:10.1029/90JA02180.

Chenette, D. L., J. F. Cooper, J. H. Eraker, K. R. Pyle, and J. A. Simpson (1980), High-energy trapped radiation penetrating the rings of Saturn, *J. Geophys. Res.*, 85(A11), 5785–5792, doi:10.1029/JA085iA11p05785.

Christon, S. P., D. C. Hamilton, G. Gloeckler, T. E. Eastman, and F. M. Ipavich (1994), High charge state carbon and oxygen ions in Earth's equatorial quasi-trapping region, *J. Geophys. Res.*, 99(A7), 13,465–13,488, doi:10.1029/93JA03328.

Christon, S. P., D. C. Hamilton, R. D. DiFabio, D. G. Mitchell, S. M. Krimigis, and D. S. Jontof-Hutter (2013), Saturn suprathermal O_2^+ and mass-28^+ molecular ions: Long-term seasonal and solar variation, *J. Geophys. Res. Space Physics*, 118, 3446–3462, doi:10.1002/jgra.50383.

Christon, S. P., D. C. Hamilton, D. G. Mitchell, R. D. DiFabio, and S. M. Krimigis (2014a), Suprathermal magnetospheric minor ions heavier than water at Saturn: Discovery of $^{28}M^+$ seasonal variations, *J. Geophys. Res. Space Physics*, 119, 5662–5673, doi:10.1002/2014JA020010.

Christon, S. P., D. C. Hamilton, J. M. C. Plane, D. G. Mitchell, R. D. DiFabio, and S. M. Krimigis (2014b), Discovery of suprathermal Fe^+ in the magnetospheres of Earth and Saturn, Abstract SM51D-4275 paper presented at 2014 Fall Meeting, AGU, San Francisco, Calif., 15–19 Dec.

Clark, R. N., et al. (2011), Composition and grain sizes of dark material in Saturn's icy satellites and rings, *EPSC Abstracts. Vol. 6, EPSC-DPS2011-1563*, EPSC-DPS Joint Meeting 2011, 2–7 Oct.

Clark, R. N., et al. (2012), The surface composition of Iapetus: Mapping results from Cassini VIMS, *Icarus*, 218, 831–860, doi:10.1016/j.icarus.2012.01.008.

Cuzzi, J., R. Clark, G. Filacchione, R. French, R. Johnson, E. Marouf, and L. Spilker (2009), Fundamental plasma processes in Saturn's magnetosphere, in *Saturn From Cassini-Huygens*, edited by M. K. Dougherty, L. W. Esposito, and S. M. Krimigis, chap. 15, pp. 459–509, Springer, Dordrecht, Netherlands, doi:10.1007/978-1-4020-9217-6_15.

DiFabio, R. D. (2012), Spatial and temporal variations of the suprathermal (3–220 keV/e) ion composition in Saturn's equatorial magnetosphere, PhD thesis, Univ. of Maryland at College Park, College Park, Md.

Estrada, P. R., and J. N. Cuzzi (1996), Voyager observations of the color of Saturn's rings, *Icarus*, 122(2), 251–272, doi:10.1006/icar.1996.0124.

Feng, W., D. R. Marsh, M. P. Chipperfield, D. Janches, J. Hoeffner, F. Yi, and J. M. C. Plane (2013), A global atmospheric model of meteoric iron, *J. Geophys. Res. Atmos.*, 118, 9456–9474, doi:10.1002/jgrd.50708.

Filacchione, G., et al. (2012), Saturn's icy satellites and rings investigated by Cassini–VIMS: III – Radial compositional variability, *Icarus*, 220, 1064–1096, doi:10.1016/j.icarus.2012.06.040.

Flandes, A., L. Spilker, R. Morishima, S. Pilorz, C. Leyrat, N. Altobelli, S. Brooks, and S. G. Edgington (2010), Brightness of Saturn's rings with decreasing solar elevation, *Planet. Space Sci.*, 58, 1758–1765, doi:10.1016/j.pss.2010.04.002.

Florescu-Mitchell, A. I., and J. B. A. Mitchell (2006), Dissociative recombination, *Phys. Lett.*, 430, 277–374.

Frankland, V. L., and J. M. C. Plane (2015), Fe embedded in ice: The impacts of sublimation and energetic particle bombardment, *J. Atmos. Sol. Terr. Phys.*, doi:10.1016/j.jastp.2014.12.004, in press.

Frisch, M. J., et al. (2009), Gaussian 09, Revision A.1, Gaussian, Inc., Wallingford CT.

Gardner, C. S., A. Z. Liu, D. R. Marsh, W. Feng, and J. M. C. Plane (2014), Inferring the global cosmic dust influx to the Earth's atmosphere from lidar observations of the vertical flux of mesospheric Na, *J. Geophys. Res. Space Physics*, 119, 7870–7879, doi:10.1002/2014JA020383.

Grebowsky, J. M. and A. C. Aikin (2002), In situ measurements of meteoric ions, in *Meteors in the Earth's Atmosphere*, edited by E. Murad and I. P. Williams, 189–214, Cambridge Univ. Press, Cambridge, U. K.

Grün, E., M. Baguhl, H. Svedhem, and H. A. Zook (2001), In situ measurements of cosmic dust, in *Interplanetary Dust*, edited by E. Grün et al., pp. 295–346, Springer, London.

Hillier, J. K., S. F. Green, N. McBride, N. Altobelli, S. Kempf, F. Postberg, J. Schwanethal, R. Srama, J. A. M. McDonnell, and E. Gruen (2007a), Interplanetary dust detected by the Cassini CDA Chemical Analyser, *Icarus*, 190, 643–654, doi:10.1016/j.icarus.2007.03.024.

Hillier, J. K., et al. (2007b), The composition of Saturn's E ring, *Mon. Not. R. Astron. Soc.*, 377, 1588–1596, doi:10.1111/j.1365-2966.2007.11710.x.

Horwitz, J. L., and T. E. Moore (1997), Four contemporary issues concerning ionospheric plasma flow to the magnetosphere, *Space Sci. Rev.*, 80(1), 49–76, doi:10.1023/A:1004973603955.

Hutchison, R. (2007), *Meteorites: A Petrologic, Chemical and Isotopic Synthesis*, pp. 1–16, Cambridge Planetary Science, Cambridge.

Jaumann, R., et al. (2009), Icy satellites: Geological evolution and surface processes, in *Saturn from Cassini-Huygens*, edited by M. K. Dougherty, L. W. Esposito, and S. M. Krimigis, chap. 20, pp. 637–681, doi:10.1007/978-1-4020-9217-6_20.

Jessberger, E. K., T. Stephan, D. Rost, P. Arndt, M. Maetz, F. J. Stadermann, D. E. Brownlee, J. P. Bradley, and G. Kurat (2001), Properties of interplanetary dust: Information from collected samples, in *Interplanetary Dust*, edited by E. Grün et al., pp. 253–294, Springer, Berlin.

Johnson, R. E., et al. (2006), Production, ionization and redistribution of O_2 in Saturn's ring atmosphere, *Icarus*, 180, 393–402, doi:10.1016/j.icarus.2005.08.021.

Jones, G. H., et al. (2006), Formation of Saturn's ring spokes by lightning-induced electron beams, *Geophys. Res. Lett.*, 33, L21202, doi:10.1029/2006GL028146.

Jurac, S., and J. D. Richardson (2007), Neutral cloud interaction with Saturn's main rings, *Geophys. Res. Lett.*, 34, L08102, doi:10.1029/2007GL029567.

Kellett, S., E. J. Bunce, A. J. Coates, and S. W. H. Cowley (2009), Thickness of Saturn's ring current determined from north–south Cassini passes through the current layer, *J. Geophys. Res.*, 114, A04209, doi:10.1029/2008JA013942.

Kempf, S., U. Beckmann, R. Srama, M. Horanyi, S. Auer, and E. Grun (2006), The electrostatic potential of E ring particles, *Planet. Space Sci.*, 54, 999–1006, doi:10.1016/j.pss.2006.05.012.

Kollmann, P. (2012), Sources, sinks, and transport of energetic particles within Saturn's magnetosphere, PhD thesis, Technische Universität Carolo-Wilhelmina zu Braunschweig, Braunschweig, Germany.

Kollmann, P., E. Roussos, C. Paranicas, N. Krupp, C. M. Jackman, E. Kirsch, and K.-H. Glassmeier (2011), Energetic particle phase space densities at Saturn: Cassini observations and interpretations, *J. Geophys. Res.*, *116*, A05222, doi:10.1029/2010JA016221.

Kopp, E. (1997), On the abundance of metal ions in the lower ionosphere, *J. Geophys. Res.*, *102*(A5), 9667–9674, doi:10.1029/97JA00384.

Krimigis, S. M., et al. (2004), Magnetosphere Imaging Instrument (MIMI) On the Cassini Mission To Saturn/Titan, *Space Sci. Rev.*, *114*, 233–329.

Krimigis, S. M., et al. (2005), Dynamics of Saturn's magnetosphere from MIMI during Cassini's orbital insertion, *Science*, *307*, 1270–1273, doi:10.1126/science.1105978.

Lindsay, B. G., and R. F. Stebbings (2005), Charge transfer cross sections for energetic neutral atom data analysis, *J. Geophys. Res.*, *110*, A12213, doi:10.1029/2005JA011298.

Lockwood, M., T. E. Moore, J. H. Waite Jr., C. R. Chappell, J. L. Horwitz, and R. A. Heelis (1985a), The geomagnetic mass spectrometer — Mass and energy dispersions of ionospheric ion flows into the magnetosphere, *Nature*, *316*, 612–613, doi:10.1038/316612a0.

Lockwood, M., M. O. Chandler, J. L. Horwitz, J. H. Waite Jr., T. E. Moore, and C. R. Chappell (1985b), The cleft ion fountain, *J. Geophys. Res.*, *90*(A10), 9736–9748, doi:10.1029/JA090iA10p09736.

Lo, H. H., L. Kurzweg, R. T. Brackman, and W. L. Fite (1971), Electron capture and loss in collisions of heavy ions with atomic oxygen, *Phys. Rev. A*, *4*(4), 1462–1476, doi:10.1103/PhysRevA.4.1462.

Luhmann, J. G., R. E. Johnson, R. L. Toka, S. A. Ledvina, and T. E. Cravens (2006), A model of the ionosphere of Saturn's rings and its implications, *Icarus*, *181*, 465–474, doi:10.1016/j.icarus.2005.11.022.

Mason, B. (1979), Data of geochemistry, Sixth Edition, Chapter B, Cosmochemistry, Part 1, Meteorites, *US Geol. Surv. Prof. Paper 440-B-1*, p. B46.

Mason, G. M., J. E. Mazur, and T. T. von Rosenvinge (1996), Energetic heavy ions observed upstream of the Earth's bow shock by the STEP/EPACT instrument on WIND, *Geophy. Res. Lett.*, *23*(10), 1231–1234, doi:10.1029/96GL01035.

Mauk, B. H., et al. (2009), Fundamental plasma processes in Saturn's magnetosphere, in *Saturn from Cassini-Huygens*, edited by M. K. Dougherty, L. W. Esposito, and S. M. Krimigis, chap. 11, pp. 281–331, doi10.1007/978-1-4020-9216-9.

Mazur, J. E., G. M. Mason, J. B. Blake, and M. C. McNab (1999), Low energy anomalous cosmic rays trapped in the Earth's magnetosphere: 6 years of SAMPEX observations, in *Proceedings of the 26th International Cosmic Ray Conference*, *7*, 527.

Mazur, J. E., G. M. Mason, J. B. Blake, B. Klecker, R. A. Leske, M. D. Looper, and R. A. Mewaldt (2000), Anomalous cosmic ray argon and other rare elements at 1–4 MeV/nucleon trapped within the Earth's magnetosphere, *J. Geophys. Res.*, *105*(A9), 21,015–21,023, doi:10.1029/1999JA000272.

Mazur, J. E., J. B. Blake, W. R. Crain, A. Y. Lin, D. J. Mabry, M. P. Zakrzewski, M. A. Turpin, and M. C. McNab (2008), New measurements of trapped anomalous cosmic rays and other heavy ions in the inner magnetosphere, Abstract U13A-0040 paper presented at 2008 Fall Meeting, AGU, San Francisco, Calif., 15–19 Dec.

Miner, E. D., R. R. Wessen, and J. N. Cuzzi (2007), *Planetary Ring Systems*, pp. 171, Springer Praxis, Chichester, U. K.

Mitchell, D. G., et al. (2005), Energetic ion acceleration in Saturn's magnetotail: Substorms at Saturn?, *Geophys. Res. Lett.*, *32*, L20S01, doi:10.1029/2005GL022647.

Mitchell, D. G., et al. (2009a), Ion conics and electron beams associated with auroral processes on Saturn, *J. Geophys. Res.*, *114*, A02212, doi:10.1029/2008JA013621.

Mitchell, D. G., et al. (2009b), Recurrent energization of plasma in the midnight-to-dawn quadrant of Saturn's magnetosphere, and its relationship to auroral UV and radio emissions, *Planet. Space Sci.*, *57*, 1732–1742, doi:10.1016/j.pss.2009.04.002.

Molina-Cuberos, G. J., H. Lammer, W. Stumptner, K. Schwingenschuh, H. O. Rucker, J. J. López-Moreno, R. Rodrigo, and T. Tokano (2001), Ionospheric layer induced by meteoric ionization in Titan's atmosphere, *Planet. Space Sci.*, *49*, 143–153, doi:10.1016/S0032-0633(00)00133-1.

Molina-Cuberos, G. J., J. J. López-Moreno, and F. Arnold (2008), Meteoric layers in planetary atmospheres, *Space Sci. Rev.*, *137*, 175–191, doi:10.1007/s11214-008-9340-5.

Moore, T. E., and G. V. Khazanov (2010), Mechanisms of ionospheric mass escape, *J. Geophys. Res.*, *115*, A00J13, doi:10.1029/2009JA014905.

Moore, T. E., et al. (1999), Ionospheric mass ejection in response to a CME, *Geophys. Res. Lett.*, *15*, 2339–2342, doi:10.1029/1999GL900456.

Moore, T. E., M. -C. Fok, and K. Garcia-Sage (2014), The ionospheric outflow feedback loop, *J. Atmos. Sol. Terr. Phys.*, *115–116*, 59–66, doi:10.1016/j.jastp.2014.02.002.

Morris, R. V., D. C. Golden, and J. F. Bell III (1997), Low-temperature reflectivity spectra of red hematite and the color of Mars, *J. Geophys. Res.*, *102*(E4), 9125–9133, doi:10.1029/96JE03993.

Moses, J. I., and S. F. Bass (2000), The effects of external material on the chemistry and structure of Saturn's ionosphere, *J. Geophys. Res.*, *105*, 7013–7052, doi:10.1029/1999JE001172.

Nagy, A. F., A. J. Kliore, M. Mendillo, S. Miller, L. Moore, J. I. Moses, I. Müller-Wodarg, and D. Shemansky (2009), Upper atmosphere and ionosphere of Saturn, in *Saturn From Cassini-Huygens*, edited by M. K. Dougherty, L. W. Esposito, and S. M. Krimigis, chap. 8, pp. 181–201.

O'Donoghue, J., T. S. Stallard, H. Melin, G. H. Jones, S. W. H. Cowley, S. Miller, K. H. Baines, and J. S. D. Blake (2013), The domination of Saturn's low-latitude ionosphere by ring 'rain', *Nature*, *496*, 193–195, doi:10.1038/nature12049.

Paranicas, C., D. Mitchell, S. Krimigis, D. Hamilton, E. Roussos, N. Krupp, G. Jones, R. Johnson, J. Cooper, and T. Armstrong (2008), Sources and losses of energetic protons in Saturn's magnetosphere, *Icarus*, *197*, 519–525, doi:10.1016/j.icarus.2008.05.011.

Plane, J. M. C. (2003), Atmospheric chemistry of meteoric metals, *Chem. Rev.*, *103*, 4963–4984, doi:10.1021/cr0205309.

Plane, J. M. C. (2012), Cosmic dust in the Earth's atmosphere (critical review), *Chem. Soc. Rev.*, *41*, 6507–6518, doi:10.1039/C2CS35132C.

Postberg, F., S. Kempf, J. K. Hillier, R. Srama, S. F. Green, N. McBride, and E. Grün (2008), The E ring in the vicinity of Enceladus II. Probing the Moon's interior—The composition of E-ring particles, *Icarus*, *193*, 438–454, doi:10.1016/j.icarus.2007.09.001.

Postberg, F., J. Schmidt, J. Hillier, S. Kemp, and R. Srama (2011), A salt-water reservoir as the source of a compositionally stratified plume on Enceladus, *Nature*, *474*, 620–622, doi:10.1038/nature10175.

Rubin, A. E. (1997), Mineralogy of meteorite groups, *Meteorit. Planet. Sci.*, *32*(2), 231–247, doi:10.1111/j.1945-5100.1997.tb01262.x.

Rubin, A. E., and J. N. Grossman (2010), Meteorite and meteoroid: New comprehensive definitions, *Meteorit. Planet. Sci.*, *45*, 114–122, doi:10.1111/j.1945-5100.2009.01009.x.

Schardt, A. W., and C. K. Goertz (1983), High-energy particles, in *Physics of the Jovian Magnetosphere*, edited by A. J. Dessler, pp. 157–196, Cambridge Univ. Press, Cambridge, U. K., and New York.

Sergis, N., S. M. Krimigis, D. G. Mitchell, D. C. Hamilton, N. Krupp, B. M. Mauk, E. C. Roelof, and M. Dougherty (2007), Ring current at Saturn: Energetic particle pressure in Saturn's equatorial magnetosphere measured with Cassini/MIMI, *Geophys. Res. Lett.*, *34*, L09102, doi:10.1029/2006GL029223.

Søraas, F. (1973), Particle observations in the magnetosphere, in *Cosmical Geophysics*, edited by A. Egeland, Ø. Holter, and A. Omholt, chap. 10, p. 146, Universitetsforlaget, Oslo.

Srama, R., et al. (2011), The cosmic dust analyser onboard Cassini: Ten years of discoveries, *CEAS Space Journal*, *2*, 3–16, doi:10.1007/s12567-011-0014-x.

Thomsen, M. F., D. B. Reisenfeld, D. M. Delapp, R. L. Tokar, D. T. Young, F. J. Crary, E. C. Sittler, M. A. McGraw, and J. D. Williams (2010), Survey of ion plasma parameters in Saturn' magnetosphere, *J. Geophys. Res.*, *115*, A10220, doi:10.1029/2010JA015267.

Tiscareno, M. S., et al. (2013), Observations of ejecta clouds produced by impacts onto Saturn's rings, *Science*, *340*, 460–464, doi:10.1126/science.1233524.

Tokar, R. L., et al. (2005), Cassini observations of the thermal plasma in the vicinity of Saturn's main rings and the F and G rings, *Geophys. Res. Lett.*, *32*, L14S04, doi;10.1029/2005GL022690.

Tseng, W.-L., W.-H. Ip, R. E. Johnson, T. A. Cassidy, and M. K. Elrod (2010), The structure and time variability of the ring atmosphere and ionosphere, *Icarus*, *206*, 382–389, doi:10.1016/j.icarus.2009.05.019.

Vandegrif, J., R. DiFabio, D. Hamilton, M. Kusterer, J. Manweiler, D. Mitchell, C. Paranicas, and E. Roussos (2012), Cassini/MIMI Instrument Data User Guide V1, NASA, Washington, D. C. [Available at http://pds.nasa.gov.]

Verbischer, A. J., M. F. Skrutskie, and D. P. Hamilton (2009), Saturn's largest ring, *Nature*, *461*, 1098–1100, doi:10.1038/nature08515.

Vondrak, T., K. R. I. Woodcock, and J. M. C. Plane (2006), A kinetic study of the reactions of Fe^+ with N_2O, N_2, O_2, CO_2 and H_2O, and the ligand-switching reactions $Fe^+.X + Y -> Fe^+.Y + X$ (X = N_2, O_2, CO_2; Y=O_2, H_2O), *Phys. Chem. Chem. Phys.*, *8*, 503–512.

Vondrak, T., J. M. C. Plane, S. Broadley, and D. Janches (2008), A chemical model of meteoric ablation, *Atmos. Chem. Phys.*, *8*, 7015–7031.

Waite, J. H., Jr., et al. (2006), Cassini ion and neutral mass spectrometer: Enceladus plume composition and structure, *Science*, *311*, 1419–1422, doi:10.1126/science.1121290.

Waite, J. H., Jr., et al. (2009), Liquid water on Enceladus from observations of ammonia and 40Ar in the plume, *Nature*, *460*, 487–490, doi:10.1038/nature08153.

Wilson, G. R., and P. D. Craven (1998), Under what conditions will ionospheric molecular ion outflow occur?, in *Geospace Mass and Energy Flow*, edited by J. L. Horwitz, D. L. Gallagher, and W. K. Peterson, AGU, Washington, D. C., doi:10.1029/GM104p0085.

Withers, P. (2012), How do meteoroids affect Venus's and Mars's ionospheres?, *Eos Trans. AGU*, *93*, 337, doi:10.1029/2012EO350002.

Yau, A. W., T. Abe, and W. K. Peterson (2007), The polar wind: Recent observations, *J. Atmos. Sol.-Terr. Phys.*, *69*, 1936–1983, doi:10.1016/j.jastp.2007.08.010.